Energy Reports 15 (2026) 109193

Contents lists available at ScienceDirect

Energy Reports

journal homepage: www.elsevier.com/locate/egyr

Research paper

Investigation of soil-based heat storage system for sustainable building heating

Sandeep Bandarwadkar[a], Tadas Zdankus[a,*], Rokas Valancius[a], Paul Christodoulides[b], Lazaros Aresti[b]

[a] *Faculty of Civil Engineering and Architecture, Kaunas University of Technology, Studentu 48–437A, Kaunas LT–51367, Lithuania*
[b] *Faculty of Engineering, Cyprus University of Technology, Archbishop Kyprianos Street 30, Limassol 3036, Cyprus*

ARTICLE INFO

Keywords:
Thermal energy storage
Seasonal energy storage
Accumulation
Soil-based
Renewable energy
Building-integrated energy storage

ABSTRACT

Seasonal heat accumulation provides various advantages. The primary benefit is the ability to generate heat with maximum capacity under optimal conditions, store the thermal energy, and retain it until the highest needs are met. Natural and environmentally sustainable resources, such as soil, are promising materials for heat storage. This study investigated the feasibility of utilising the thermal energy generated by solar collectors from spring to autumn to heat a private building during the cold period. The proposed method involved storing heat in the soil beneath the building, isolating it from the surrounding ground. Heat dissipation in a limited soil volume was experimentally studied. The high inertia of the processes and changes in soil temperature fields, depending on the charge level of the thermal energy storage system, complicate the assessment of its state. Numerical studies have shown that the average soil temperature of the accumulator is more suitable for controlling the connection of solar collectors to the storage system than the outlet fluid temperature of the heating device, which is currently the primary method used in practice. Depending on the charge level, defined by the average soil temperature, the daily operating time of solar collectors for soil charging decreases, reducing the charging potential. In June, this reduction is less than one per cent, while in less favourable periods, such as September, it can reach about five per cent. This should be taken into account in design calculations.

1. Introduction

The increasing demand for sustainable energy solutions has driven extensive research into thermal energy storage (TES) systems to balance energy supply and demand effectively (Bogdanov et al., 2021). According to the International Energy Agency (IEA), total global energy supply is projected to rise by 30% between 2020 and 2050 in their STEPS scenario. While energy consumption is emerging and developing econiomies is expected to grow by approximately 50%, driven by economic growth and population expansion ("Net Zero by, 2050: A Roadmap for the Global Energy Sector", 2025). In 2022, global electricity demand increased by 2.4%, following a record 6% increase in 2021 ("Global electricity demand growth is slowing, weighed down by economic weakness and high prices - News - IEA.", 2025). The share of renewable energy in the global electricity mix is projected to grow from 29% to 35% by 2025, intensifying the need for efficient storage systems to manage intermittency associated with solar and wind resources ("Executive summary – Electricity Market Report, 2023 – Analysis - IEA.", 2025). Accordingly, the International Renewable Energy Agency projects that the deployment of energy storage, including TES, must grow 17 times by 2030 to support the widespread integration of renewables ("Tripling renewable power and doubling energy efficiency by, 2030: Crucial steps towards 1.5°C.",2025).

Seasonal thermal energy storage systems have garnered considerable attention among various thermal energy storage systems. These systems capture and store energy during periods of excess supply, such as summer, and supply it when demand is higher, such as during winter (Bolton et al., 2023). Thermal energy storage technologies are broadly classified into three main mechanisms: sensible heat storage, latent heat storage, and thermochemical storage (Yang et al., 2021; Arabkoohsar, 2023). Sensible heat storage using materials such as rock, water, and soil has been extensively explored due to its reliability and technological maturity, although realistic modeling on underground boundary conditions and long-term heat losses remains critical for improving

---

* Corresponding author.
E-mail address: tadas.zdankus@ktu.lt (T. Zdankus).

https://doi.org/10.1016/j.egyr.2026.109193
Received 2 December 2025; Received in revised form 6 February 2026; Accepted 8 March 2026

efficiency (Saleem et al., 2022; Koçak et al., 2020). Latent heat storage (LHS) leverages phase change materials and offers a higher density by storing the heat during material phase transitions (Salunkhe and Jaya Krishna, 2017). Despite its promise, LHS systems are currently suited to short-term applications due to the stability issues of PCMs over long periods (Jouhara et al., 2020). In contrast, thermochemical storage presents high storage potential with minimum thermal losses, as it relies on reversible chemical reactions (Bao and Ma, 2022). Though feasibility studies have demonstrated their effectiveness in smaller-scale, short-term settings, they are still under development for large-scale, seasonal applications (Steinmann, 2021).

Sensible heat storage technologies stand out for their simplicity, cost-effectiveness, and advancement compared to other alternatives (Seyitini et al., 2023). Among these underground thermal energy storage (UTES) systems, such as the aquifer thermal energy storage systems (ATES) and the borehole thermal energy storage (BTES) systems, are particularly notable for practical application (Brown et al., 2024). ATES systems store thermal energy in natural groundwater reservoirs through seasonal injection (Pourahmadiyan et al., 2023). ATES is especially prevalent in countries such as the Netherlands, which hosts 85% of global ATES installations, and Sweden, with Belgium and Denmark, hosting about 9% of global ATES systems (Fleuchaus et al., 2018). With storage capacities ranging from 10 GWh to over 100 GWh, ATES is a key player in district heating and cooling applications (Sadeghi et al., 2024). However, its deployment is limited by the availability of suitable aquifers and the need for strict environmental management (Stemmle et al., 2024). The Borehole Thermal Energy Storage (BTES) system offers an alternative approach by utilising vertical wells drilled into the ground, typically between 50 and 150 m deep, where heat exchangers circulate fluid to store heat in the surrounding rock or soil. The storage heat is recovered during winter to meet the demand (Ahmadfard and Baniasadi, 2025). Notable implementations such as the Drake Landing Solar community in Canada demonstrate a high solar fraction approaching 90%with capacities between 5 and 30 GWh. BTES is widely used for residential and district heating in suburban and rural regions (Sibbitt et al., 2012). However, these systems are challenged by high installation costs due to drilling and the complexity of networked heat exchangers, which can impact their economic feasibility for smaller applications (Lanahan and Tabares-Velasco, 2017; Sass et al., 2024).

Pit Thermal Energy Storage (PTES) systems use large insulated pits filled with water or gravel-water mixtures. Solar collectors heat water in summer and winter, extracting stored heat to meet heating demands (Sadeghi et al., 2024). PTES systems are increasingly popular in Scandinavian countries such as Denmark, where district heating networks integrate them seamlessly. For example, the Master PTES plant in Denmark, with a storage capacity of 75,000 m^3, plays a crucial role in meeting local heating requirements ("Large Scale solar heating in Marstal.", 2025). Despite their growing adoption, PTES systems require significant land and incur upfront costs for excavation and water management, making them less suitable for areas with limited surface (Xiang et al., 2022). Tank thermal energy storage (TTES) systems use insulated tanks filled with water, often above the ground. During summer, excess heat from solar collectors or other sources heats the water in tanks, and in winter, this heat is released to provide heating (Hua et al., 2023). TTES has been successively implemented in industrial and small-scale heating applications, with a capacity ranging from 1 to 20 GWh. One notable example is the Vojens solar district heating system in Denmark, which features a 13,000 m^3 tank to sustain the network ("Large-scale thermal storage pit.", 2025). However, TTES systems face challenges such as limited scalability, aesthetic constraints, and zoning restrictions, which may constrain their wider adoption (Sarbu and Sebarchievici, 2018).

The soil is increasingly recognised as a viable medium for thermal energy storage due to its availability, cost-effectiveness, and substantial heat retention capabilities (2016 7th India International Conference on Power Electronics IICPE, 2016). Thermal performance is strongly influenced by soil type, moisture content, and environmental conditions, affecting conductivity, heat capacity, and density (Abu-Hamdeh and Reeder, 2000a). Compared with conventional storage media, soil enables scalable and building-integrated seaspnal storage concepts, making it an innovative option for enhancing energy efficiency in various systems (Tawalbeh et al., 2023). As for underground Thermal Energy Storage using soil, many authors have studied underground energy dynamics to evaluate the feasibility of using the soil as an option for seasonal heat storage (Walker et al., 1979; Gabrielsson et al., 2000; Zhang et al., 2015a).

K. Xiong et al (Xiong et al., 2023). researched a model to accurately estimate soil thermal conductivity based on soil saturation, addressing the challenges of time and effort in obtaining this key parameter for applications like heat pumps, groundwater withdrawal, and soil-based heat storage. The model uses a linear expression for dry soil thermal conductivity and a geometric mean for saturated soil conductivity, with a quadratic function to cover values between these limits. When tested against five established models and measured data from 51 soil samples, ranging from sand to silty clay loam, the model showed strong accuracy, proving effective across diverse soil types and moisture levels. In related research, solar-ground coupled heat pumps with a seasonal storage system in cold regions. The researchers calculated soil temperature distribution and thermal influence radius of storage wells using a line heat source model and FLUENT software under various soil conditions during the non-heating season. Also, different types and sizes of sand affect the thermal conductivity of backfill material. Results indicate that heat initially diffuses quickly in the soil but slows as storage time increases (Zhou et al., 2021).

The effects of water phase changes on soil thermal properties were discussed by various authors, emphasising the interaction between moisture and heat transfer. Multiple algorithms have been studied to assess soil heat exchange and storage capabilities, with the Duct Ground Heat Storage model being the most prominent. Originally developed by Hellstrom in 1989, the Duct Ground Heat Storage model was adapted for TRNSYS simulations by Nordell and Hellstrom in 1996. While complex in structure, Duct Ground Heat Storage is computationally efficient and has become a benchmark method for simulating underground heat storage systems, particularly suited for modelling large, compact heat storage setups with underground tubes (Sarlos et al., n.d). Transport of Unsaturated Groundwater and Heat (TOUGH) was developed by researchers at Lawrence Berkeley National Laboratory, which codes to study subsurface heat flow in porous media ("TOUGH: Suite of Simulators for Nonisothermal Multiphase Flow and Transport in Fractured Porous Media - TOUGH.", 2025). Pruess later expanded TOUGH to include equations to solve multiphase and multicomponent heat flow. However, its application to high-temperature ground thermal energy storage systems (up to 90 °C) remains unexplored (Pruess, 2004). An integrating modelling platform, GeoSiam, has been employed to examine fluid dynamics, geochemistry, and geomechanics in geothermal storage. Perego analysed a borehole thermal energy storage using GeoSiam in 15 vertical boreholes, identifying thermal imbalance due to varied geological layers, particularly those with low thermal properties (Chapuis and Bernier, 2009; "User Manual for GeoSIAM Software Version 2.0 - RSE.", 2025).

To solve energy imbalance and reduce heating costs, underground insulated thermal energy storage systems are increasingly being explored for residential heating applications. A study has investigated solar-assisted shallow soil storage beneath the greenhouses, showing moderate thermal performance across growing seasons. However, the application was restricted to agricultural use and short-term buffering rather than long-duration seasonal storage (Zhang et al., 2015b). Another study of underground soil-based TES of 900 m^3 for a Danish housing project was analysed. The system was charged via PV-power air-source heat pump, demonstrating seasonal storage feasibility, but in a building-scale context with different boundary conditions than insulated and without direct solar-thermal coupling (Jradi et al., 2017).

Recent reviews have emphasized the importance of compact, well-insulated storage concepts capable of direct integration with solar thermal systems under real climatic boundary conditions. These works collectively highlight the need for enhanced system-level optimisation, including control strategies and realistic boundary conditions, to improve seasonal efficiency and reduce auxiliary energy demand (I. I. Renewable Energy Agency, 2025; "“Technology Position Paper Compact Thermal Energy Storage,” 2023; Vahidhosseini et al., 2024). However, detailed experimental validation of compact soil-based TES systems under seasonal operating conditions remains limited.

Also, existing studies have focused on improving sensible, latent, and thermochemical storage mechanisms and simulating subsurface heat transfer using models like DST and TOUGH (Sarbu and Sebarchievici, 2018). However, limited research has explored the precise thermal behaviour of soil-based TES systems under variable environmental conditions, particularly regarding seasonal charging and discharging cycles (Jradi et al., 2017). Additionally, most studies have emphasised theoretical modelling, with few experimental investigations addressing short-term heat accumulation and dissipation in controlled conditions representative of real applications (Ji et al., 2024).

This paper systematically investigates the thermal performance and seasonal heat storage potential of a soil-based thermal energy storage system through experimental analysis and numerical modelling. While conventional large-scale systems such as borehole or aquifer storage are well established for district-scale applications, they typically require specific site conditions and substantial drilling or groundwater access, limiting adoption at the building scale. A key research gap lies in the experimentally validated characterization of insulated, building-integrated soil TES systems operating under realistic climatic conditions with practical charging and discharging control strategies.

Therefore, this study addresses that gap by performing controlled experiments to characterize transient heat accumulation and dissipation across soil layers, and coupling analytically derived solar-collector outlet temperatures to a 3D-1D COMSOL model of an insulated, below-building TES for a representative A+ class dwelling in Kaunas, Lithuania. The research demonstrates the possibility of capturing and storing surplus solar energy during summer, when heating demand is minimal, for use in winter. This approach provides a cost-effective and adaptable solution to enhance renewable energy utilization in buildings while reducing dependence on fossil-fuel-based heating systems.

2. Experimental setup and methodology

The experiment involved analysing and simulating heat transfer and its accumulation through different soil layers with a single fraction and moisture content (Figs. 1 and 2), contained within the box lined with thermal insulation. The box (Fig. 2, (a)), a thermal energy storage system, was constructed by excavating a rectangular volume of 0.25 m^3 from the ground. The TES volume was filled with sand with 10% moisture content. The TES was sealed in its entirety, preventing surrounding groundwater from altering the soil's characteristics. The horizontal cross-sectional area of the TES was equal to 0.25 m^2, measuring 0.5 m in both length and width. The inside height of the soil in the TES, excluding the thickness of thermal insulation, was one meter. The thermal insulation layer was made of extruded polystyrene EPS 70 NEO with a thickness of 0.05 m. Because the TES enclosure was fully sealed using a double-layer polystyrene film of 0.0002 m thick, groundwater movement throughout the storage volume was prevented, resulting in a closed experimental system with no mass exchange with the surrounding ground. Consequently, advective heat transport was absent, and heat transfer occurred solely within the enclosed soil and insulation boundaries.

A dedicated heating device charged the TES (Fig. 2(c)). It featured two Backer AB tubes arranged in series, each with a length and diameter of 1.6 m and 0.0085 m, respectively. The heating tubes were connected to the single-phase electrical network of 220 V. The steel plate served as a heating surface, with dimensions equal to the base of the TES and a thickness of 0.001 m. It was securely mounted onto the heating tubes,

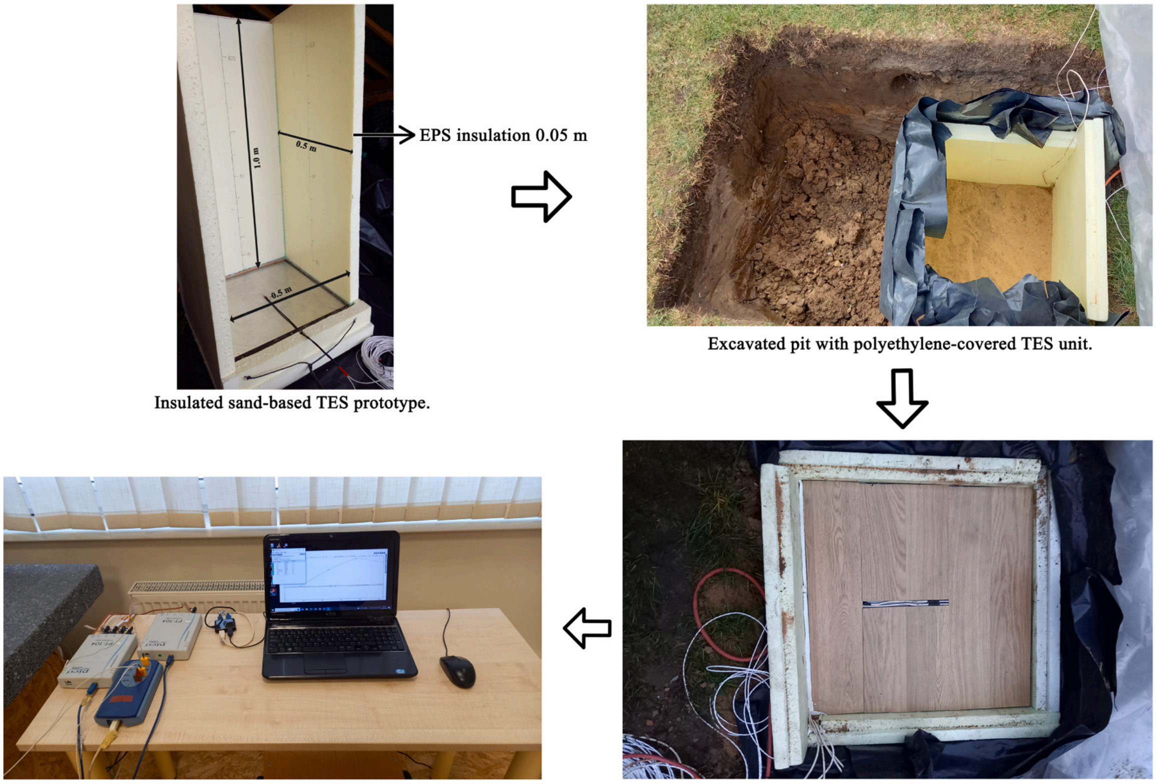

Insulated sand-based TES prototype.

Excavated pit with polyethylene-covered TES unit.

Closed TES with embedded temperature sensors.

Data acquisition and monitoring system.

Fig. 1. Construction and installation of TES and connection to the data acquisition system.

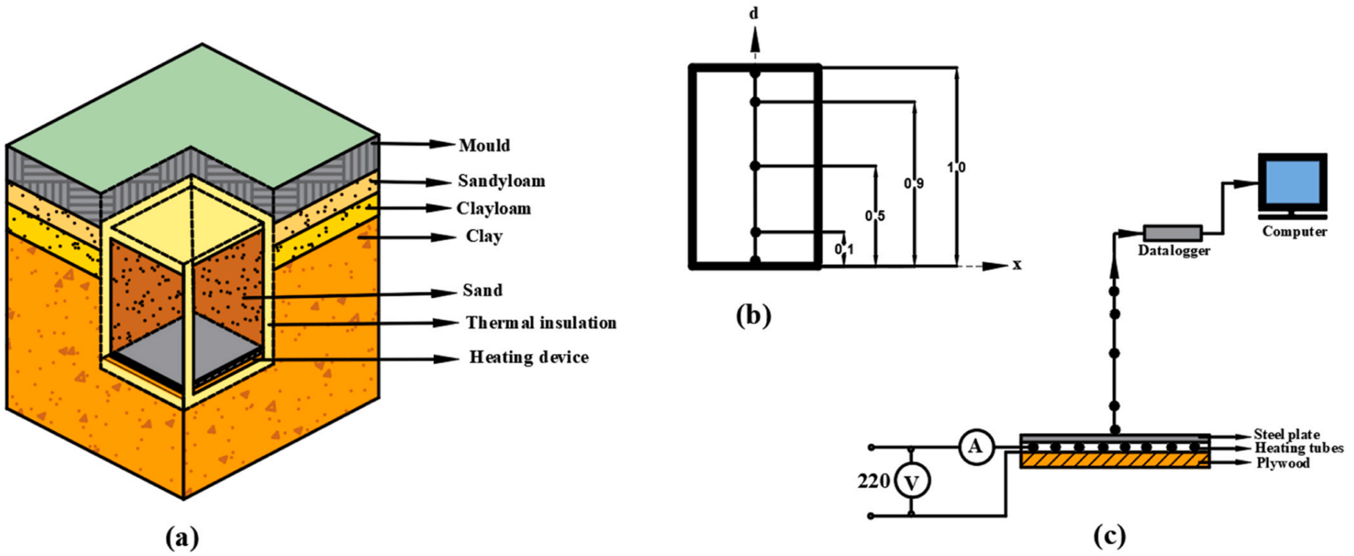

Fig. 2. Schematic representation of experimental setup: (a) TES position under the ground, (b) position of the temperature sensors, (c) scheme of the heating device.

ensuring complete contact between the plate and the tubes. The heating surface and tubes were positioned on a foundation made of plywood coated with a film layer, 0.012 m thick. This heating device was placed beneath the soil at the bottom of the TES. The heating tubes and cables' total electrical resistance (R) was $R = 71.83\ \Omega$. It was assumed that the electrical energy of the heating device was fully converted to heat at the outlet. The heating process was applied in a controlled and repeatable manner with the TES charged over defined experimental periods to observe transient heat accumulation behaviour. Therefore, the thermal power (P) of the heating device was calculated using Eq. (1):

$$P = \frac{U^2}{R}. \tag{1}$$

Where:

P – Thermal power [W].

R – The electrical resistance [Ω].

U – Voltage [V].

The heat was transferred from the heated surface to the overlying soil layers above. For a more detailed examination of this upward heat transfer, the entire volume of TES was conceptually divided into k horizontal layers, each labelled with index m, increasing sequentially from $m = 1$ to k. This analysis was conducted under the condition that the temperature of the soil layers remained below 100 ℃ and no phase change occurred. The thermal conductivity of sand was treated as spatially uniform and constant over the entire TES volume. No forced airflow or fluid circulation was applied during the experiment; therefore, the heat transferred to any given soil layer was due to conduction and can be described by the heat flux density, q [W/m^2], and expressed as Eq. (2):

$$q = -\lambda \frac{\left(T_{(m),t} - T_{(m+1),t}\right)}{\delta}. \tag{2}$$

Where:

λ – The thermal conductivity of the sand [W/(m K)], which was assumed to remain constant throughout the entire volume within the TES.

δ – Inside height of the soil in the TES [m].

$$\delta = \frac{h}{k_{soil,l}}. \tag{3}$$

Where:

h – The thickness of the layer [m], expressed as (Eq. (3)):

$k_{soil,l}$ – The number of the specific soil layers within TES [dimensionless].

$T_{(m),t}$ – The temperatures of the soil layers at the moment t [K].

The temperature measurements were taken using temperature sensors of TJ1-Pt1000/A, operating within a range of −30–180 ℃ and using a three-wire connection type. The sensor was positioned at the centre axis of the heated surface and had a vertical distance from the surface (Fig. 2) of 0.1, 0.5, 0.9, and 1 m. Data readings were recorded via the PT-104 Data Logger, offering a resolution of 0.001 ℃ and an accuracy of 0.015 ℃. This ensures the recorded data remains highly precise within the specified operating conditions.

The average temperature change per hour, $\Delta T_{avg,h}$ over time, was calculated to capture the temperature increase or decrease trend across multiple intervals and was expressed as (Eq. (4)):

$$\Delta T_{avg,h} = \frac{1}{n}\sum_{i=1}^{n}\left(T_{t_{(i)}} - T_{t_{(i-1)}}\right). \tag{4}$$

Where:

i – Index that represents the time step from 1 to n [–].

$T_{t(i)}$ – The temperature at time t [K].

n – Total number of time points considered [–].

The increase in the temperature ($\Delta T_{st,d}$) in the soil layers for each day was determined using Eq. (5):

$$\Delta T_{d_x} = T_{d_x,end} - T_{d_x,initial}. \tag{5}$$

The subscript "end" represents the temperature at the end of the day, and "initial" represents the beginning of the same day.

With no specific heat-discharged equipment installed, the TES was designed to self-discharge through natural heat loss to the surrounding environment. For this reason, a thinner layer of insulation was selected around the TES. The thermal properties of different materials at a moisture content of 10% used in the simulation are listed in Table 1. It should be noted that the reported temperature evaluation and short-term heat accumulation behaviour correspond to a controlled baseline moisture content of 10%. Since soil thermal conductivity and volumetric heat capacity are moisture dependent, quantitative results such as penetration depth, response lag, and accumulation rate may vary under different moisture conditions.

The experimental analysis was conducted under climatic conditions characteristic of Kaunas, Lithuania.

The average monthly meteorological data, including temperature, relative humidity, and wind speed, are given in Fig. 3 ("Technical

Table 1

Thermal properties of the material used in the experimental setup and simulations (“Home - Lithuanian Geological Survey under the Ministry of Environment.” 2025; Abu-Hamdeh and Reeder, 2000b).

Material	Thermal conductivity [W/m. K]	Density [kg/ m^3]	Specific heat capacity [J/kg. K]
Mould	0.45	1300	1800
Sandy loam	1.20	1600	850
Clay loam	0.55	1400	1400
Clay	0.8	1900	1500
Extruded polystyrene	0.036	28	1300
Steel plate	50	7.85	490
plywood	0.12	500	1700
Sand	1.45	1800	1200

Regulations for Construction, STR 2.01.12:2024, Construction Climatology"", 2025).

3. Computational model

3.1. Boundary conditions for the numerical simulations

The model design and simulation were conducted in two stages to assess the TES system integrated with solar energy. In the first stage, the boundary conditions for the thermal energy storage model were defined based on the calculated outlet temperature of the solar thermal collectors, which were derived analytically using standard equations considering solar irradiance, collector efficiency, and heat loss coefficient. In the second stage, these outputs were incorporated into a COMSOL Multiphysics (v 6.1) model to evaluate the feasibility of storing the harvested energy in a soil-based TES system beneath a residential building. The study focused on a 120 m^2 single-family house in Kaunas of a high energy efficiency class (“Technical Regulations for Construction, STR 2.01.02:2016, Energy Performance Design and Certification of Buildings”, 2025). This building was selected as a representative case study, reflecting Lithuania's housing characteristics, where the average functional area per dwelling is 68.4 m^2, with private ownership dominating at 98.6% (“Housing - Oficialiosios statistikos portalas.”, 2025).

In the cold season, a building of the aforementioned energy efficiency class consumes an average of about E_{Bh}= 6.5 MWh of thermal energy for heating (“Technical Regulations for Construction, STR 2.01.12:2024, Construction Climatology"", 2025; “Technical Regulations for Construction, STR 2.01.02:2016, Energy Performance Design and Certification of Buildings”, 2025). It was assumed that the annual heat loss from the heat storage system to the environment would not exceed thirty per cent of the total thermal energy consumed for heating (Mangold and Deschaintre, 2025). In this case, E_{st}= 9.3 MWh of heat needs to be charged into the heat storage system. Solar radiation in Lithuania is sufficient to generate significant amounts of heat (>300 MJ/m^2) during the period from March to September inclusive. Then, the monthly average amount of energy from solar radiation falling on a surface inclined at an angle of 40° per m^2, starting from March, is: 355, 474, 612, 585, 589, 528, and 405 MJ/m^2. In total, this is 3548 MJ/m^2, which corresponds to E_M= 985.6 kWh/m^2.

The solar thermal system analysed for the selected building employs a solar thermal setup (Fig. 4) to supplement building heating demand (Kveselis et al., 2014). Premium-quality flat plate solar collectors (FPCs) were selected for medium-temperature applications (30–80 °C), which aligns with the operational range of the TES system (Kalogirou, 2004).

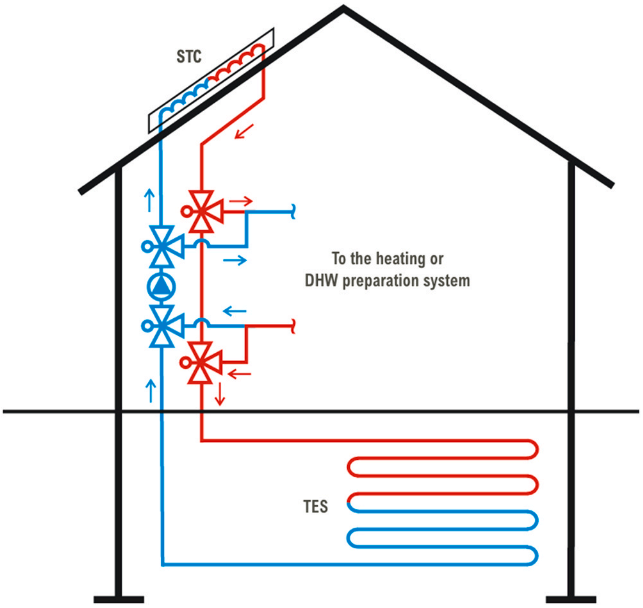

Fig. 4. Scheme of TES coupled with Solar Thermal Collector (STC).

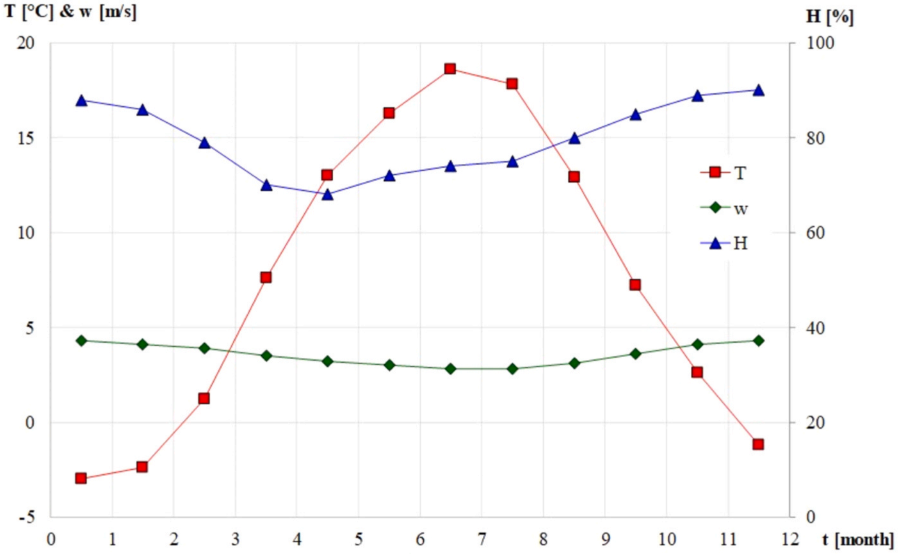

Fig. 3. Average monthly air temperature, relative humidity, and wind velocity for Kaunas, Lithuania.

Each collector has a total gross area of 2.0 m^2, with an aperture and absorber area of A_{coll}= 1.8 m^2, reflecting an optimised design where nearly all incident solar radiation is effectively transmitted and absorbed without significant edge losses. The collectors are installed at a tilt angle of 40°, slightly lower than the latitude of Kaunas (54.9°) ("Solar Tilt Angle: How To Find The Best Panel Position.", 2025), and oriented southward (0° azimuth) to enhance annual solar capture, particularly during the summer season, which is advantageous for seasonal heat storage ("IEA SHC et al., 2025). The absorber is coated with a spectrally selective surface (absorptance τ_α =0.95, emittance < 0.1) to maximise solar radiation while reducing inferred radiation losses (Xu et al., 2020). The glazing consists of low-iron, tempered glass with a transmittance of 0.90, ensuring high solar transmittance while minimising convective and radiative losses ("EN 12975-1:2006 - Thermal solar systems and components - Solar collectors - Part 1: General.", 2025). Rear and side insulation is provided using mineral wool or polyurethane foam (0.035 W/m.K) to minimise heat loss to ambient air (Kalogirou, 2004). Collector performance was modelled using validated coefficients derived from the ISO 9806/solar keymarks test, allowing accurate prediction of thermal output. For TES charging calculations, an average operating point collector efficiency of η_{coll}= 0.53 was adopted based on the ISO 9806 efficiency model at a reference irradiance of 1000 W/m^2 and a mean temperature difference between collector fluid and ambient air of 45 K. This efficiency was computed from certified flat-plate parameters (gross area: η_o=0.76, $a_1 = 4.07$ W/m^2.K, $a_2 = 0.02$ W/m^2.K^2) and aligns with EU/keymark practice for reporting collector effciecincy ("GUIDE TO STANDARD ISO, 9806:2017 A Resource for Manufacturers, Testing Laboratories, Certification Bodies and Regulatory Agencies," 2018; SP Technical Research Institute of Sweden, 2010; Duuzaamloket," Solar collector energy label values,", 2017).

The total absorber area of collectors A is calculated by Eq. (6):

$$A = \frac{E_{st}}{E_M \eta_{coll}}. \tag{6}$$

Where:

E_{st} – The energy to store [kWh].

E_M – The energy of solar radiation per square meter [kWh/m^2].

η_{coll} – An average field efficiency of solar collector [–].

The total required absorber area of the collectors is equal to A= 17.8 m^2. The necessary number of collectors, k_{coll}, should be at least: $k_{coll} \geq A/A_{coll}$. This means that at least ten collectors of the aforementioned type are needed to produce the entire amount of thermal energy required for heating the building (E_{st}).

The volume of the heat storage (V) is related to the maximum amount of heat (E_{st}) that needs to be charged to the heat accumulator. The sand was selected as the ground type filler for heat storage, as in the experimental part. The sand's moisture content, density, and heat capacity were respectively equal to: μ_{soil}= 10%, ρ_{soil}= 1800 kg/m^3, and $c_{p,soil}$= 1200 J/(kgK). The change in the filler's temperature ΔT, is a crucial parameter for operating the heat storage system over an extended period. A lower temperature gain is desirable because the heat loss through the storage walls to the environment depends on the temperature difference between the filler at the storage site and the surrounding medium outside. In this research, the requirement was set that the temperature increase ΔT should be near 50 ± 2.5 ℃. By choosing the dimensions of the heat tank, the length (L), width (W), height (H), respectively equal to: L= 12 m, W= 10 m, H= 2.5 m, the volume of the tank was equal to: $V=L\times W\times H$= 300 m^3. A verification calculation was performed: $\Delta T_{soil}=E_{st}/(\rho_{soil}Vc_{p,soil})$= 51.7 ℃.

The next question is how to charge the heat accumulator with heat (Fig. 5). It is necessary to ensure the required intensity of heat exchange. The thermal accumulator charging system must be designed to store all the heat generated by the solar collectors. The fluid is heated in the solar collectors and, as a heat carrier, transports the thermal energy to the storage tank. A propylene mixture (33.3% concentration), ensuring stable performance in varying climatic conditions ("Heat Transfer Fluids for Solar Water Heating Systems, Department of Energy." 2025; Fan et al., 2007), was chosen for circulation in the heat storage system: ρ_{fl}= 1034 kg/m^3, $c_{p,fl}$= 3600 J/(kgK). The circuit operates at a pressure of four bars in the system loop, with a total fluid volume of 19.8 litres and an average flow rate of G= 288 litres/h ("Heat Transfer Fluids for Solar Water Heating Systems, Department of Energy." 2025). When exposed to solar radiation in the collectors, the liquid is heated, and its temperature is raised (Fig. 4). In this case, it is necessary to know the distribution of solar radiation intensity during the day. At the peak moment, which is 13:00, in Kaunas, Lithuania, the maximum power of solar radiation is $P_{sol,\ rad,\ max} = 650$ W/m^2 (Duuzaamloket," Solar collector energy label values,", 2017). In total, for ten collectors, it is equal to $P_{coll,max}=k_{coll}A_{coll}\eta_{coll}P_{sol,\ rad,max}$= 10•1.8•0.53•650 = 6.2 kW.

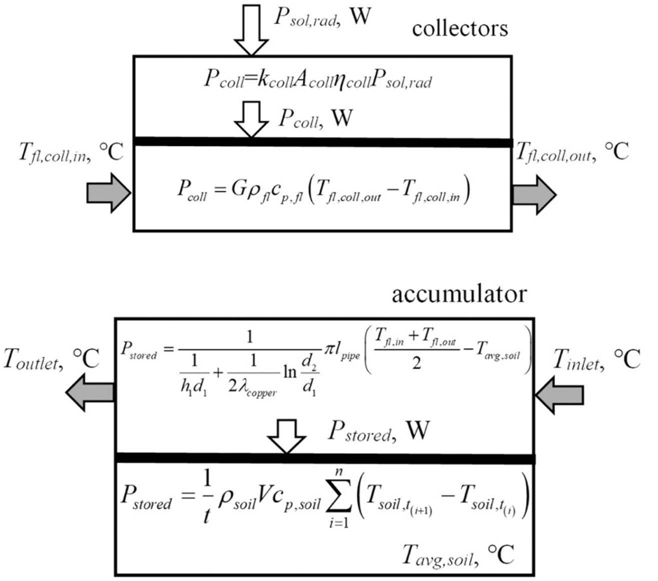

Fig. 5. Energy conversion and heat transfer diagram in solar collectors and the thermal accumulator.

$P_{coll,max}$ corresponds to the maximum amount of energy transferred to the fluid circulating in the system (Fig. 4). It is possible to calculate how much the temperature of the fluid $\Delta T_{fl,coll}=T_{fl,coll,out}$-$T_{fl,coll,in}$ will change (Eq. (7)):

$$P_{coll} = G\rho_{fl}c_{p,fl}\left(T_{fl,coll,out} - T_{fl,coll,in}\right). \tag{7}$$

At the peak moment, the power of the solar radiation reaches its maximum $P_{coll,max}$. Then the fluid flowing through the collectors is heated to its maximum, and the change in fluid temperature is at its highest: $\Delta T_{fl,coll,max}$= 20.8 ℃ (Eq. 7). Outflowing from solar collectors, the fluid moves to a tubular heat exchanger placed in the heat storage tank. It was assumed that all the heat carried by the fluid was transferred to the ground filler and evenly distributed in it, and the temperature of the outflowing fluid from the accumulator was approximately equal to the average temperature of the ground filler.

Based on the amount of energy transferred to the sand, it is possible to estimate the average increase in soil temperature. The change in temperature of the accumulator's filler over time was calculated by Eq. (8):

$$P_{stored} = \frac{1}{t}\rho_{soil}Vc_{p,soil}\sum_{i=1}^{n}\left(T_{soil,t_{(i+1)}} - T_{soil,t_{(i)}}\right). \tag{8}$$

Where:

$T_{soil,t(i)}$; $T_{soil,t(i+1)}$ – The soil temperature at the $(i)^{th}$ and $(i+1)^{th}$ moments of time t [K].

It should be noted that the temperature of the soil filler in the accumulator's volume increases unevenly. At the hot fluid inflow zone, the soil temperature is higher, and at the outflow zone, it is lower. For a deeper analysis, to determine the temperature fields in various sections of the accumulator at various times, it is necessary to perform a numerical simulation.

All the generated heat is stored in the accumulator. It is essential to ensure that the heat exchanger can maintain the required heat exchange intensity. First, the material and diameter of the heat exchanger contour, i.e., the pipe, must be selected, and then its length must be calculated. Copper was chosen for better heat transfer (λ_{copper}=390 W/(mK)). The copper pipe DN20 with a wall thickness of 1 mm, d_1= 0.020 m (inner diameter of the pipe), d_2= 0.022 m (outer diameter of the pipe)) was selected. Regarding the laminar flow regime, the value of the internal heat transfer coefficient from the fluid to the inner side of the pipe's wall was not high and was approximately equal to h_1= 70 W/(m^{2}K). Temperatures: $T_{inlet}=T_{fl,in}=T_{fl,coll,out}$= 35.8 °C, and $T_{outlet}=T_{fl,out}\approx T_{avg,soil}$ were used in calculations. Having the $P_{stored}=P_{coll,max}$= 6.2 kW, the length l_{pipe} of the pipe was calculated by Eq. (9):

$$P_{stored} = \frac{1}{\frac{1}{h_1 d_1} + \frac{1}{2\lambda_{copper}} \ln\frac{d_2}{d_1}} \pi l_{pipe} \left(\frac{T_{fl,in} + T_{fl,out}}{2} - T_{avg,soil}\right). \tag{9}$$

It may be concluded that the length of the heat exchanger's pipe needs to be no less than l_{pipe}= 78.8 m.

3.2. Methodology of the numerical simulations

To define the boundary temperature profile of the solar collector outlet for the numerical model, hourly outlet temperatures were calculated using analytical formulations based on incident solar radiation and collector thermal characteristics. The flat plate collectors used in this study were defined by an absorber area of 1.8 m^2, a field efficiency of 53%, a transmittance value of 0.90, a selective surface absorptance of 0.95, and a thermal loss coefficient of 4.5 W/[m^2 K]. A 33.3% propylene mixture circulated through the loop at four bar pressure and 288 l/h flow rate, consuming 10.5 kWh of auxiliary energy per year.

Representative hourly solar irradiance data for Kaunas, Lithuania, were obtained from the PVGIS database ("JRC Photovoltaic Geographical Information System PVGIS - European Commission.", 2025). The data include direct normal irradiance (DNI), diffuse horizontal irradiance (DHI), and the resulting global tilted irradiance on a 40° south-facing surface. For Kaunas, the typical annual global tilted irradiance is around 1150–1250 kWh/m^2, with DNI contributing about 65% and DHI about 35% of this total (María and Huld, 2013; "PVGIS data sources and calculation methods - European Commission.", 2025). They were used directly in the thermal power (P_{coll}) calculations using $P_{coll}=k_{coll}A_{coll}\eta_{coll}P_{sol,rad}$ without further decomposition. During the dark period, solar radiation was zero. Therefore, the fluid circulation was stopped at night. Due to heat losses to the environment, the liquid temperature in the collectors decreased to a value close to the atmospheric air temperature.

A 3D TES model measuring 12 m in length, 10 m in width, and 2.5 m in depth was created in COMSOL with a foundation of 0.3 m thickness. Only the interface between the flooring and the sand layer was included in the model (Fig. 6). The foundation was enclosed with a 0.1 m-thick insulation layer, and the enclosed space was filled with sand. Copper heating pipes with a diameter of DN20 were horizontally positioned in three layers at depths of 0.625 m (first layer), 1.25 m (second layer), and 1.875 m (third layer) below the flooring. The pipes were spaced 1 m apart and arranged with a turning radius of 1 m, with a total pipe length of 390 m. The TES domain, insulation, and foundations were explicitly modelled as separate solid regions using the thermal properties listed in Table 1 to ensure accurate representation of conductive heat transfer across material interfaces. The heating pipe dimensions and layout were selected based on recommendations for efficient heat transfer, uniform thermal distribution, minimised pressure losses, and ease of maintenance, aligned with copper pipe standards and thermal efficiency guidelines ("Applications: Tube, Pipe and Fittings: Copper Tube Handbook: III. Solar Energy Systems.", 2025).

To accurately capture the TES system's thermal dynamics, COMSOL Multiphysics was used to analyse heat transfer mechanisms within both the solid domain (TES unit) and the piping network (Fig. 6). The convection-diffusion equation was utilised within the heat transfer in the COMSOL Multiphysics solids module, with a one-dimensional piping network modelled using the heat transfer in the pipes module. The temporal heat distribution was governed by the general heat transfer equation derived from the energy balance principle. Consequently, the three-dimensional transient heat conservation equation for an incompressible fluid can be expressed as Eq. (10):

$$Q_e = \rho c_p \frac{\partial T}{\partial t} + \nabla q. \tag{10}$$

Where:

Q_e – An external heat source [W/m^3].
ρ – The density of the sand [kg/m^3].
c_p – The specific heat capacity of the sand [J/kg•K].
T – The temperature [K].
t – The time [s].

Based on the above equation, it can be interpreted that energy balance within the fluid flow in the buried pipe accounts for the internal energy change, convective transport, conductive redistribution to the surrounding sand, and frictional losses. Simulating full-scale geometries with the inclusion of the piping network can be challenging due to the large discrepancy in the scale of the domain and the pipe diameter. The high aspect ratio means that employing equilateral cells in the mesh would demand significant computational power and memory. Existing computational methods address this challenge either by using a coordinate scaling approach (Aresti et al., 2024; "Computational modelling of a ground heat exchanger with groundwater flow.", 2025) or, as applied here, by adopting a 1D approach coupled with the 3D domain (Aresti et al., 2020), and expressed as Eq. (11):

$$\nabla_t (Ak\nabla_t T) + 0.5 f_D \frac{\rho A}{d_h} |u| u^2 = \rho A c_p \frac{\partial T}{\partial t} + \rho A c_p u e_t \nabla_t T. \tag{11}$$

Where:

A – The cross-sectional area of the pipe [m^2].
f_D – Friction factor [–], which was estimated using the Churchill

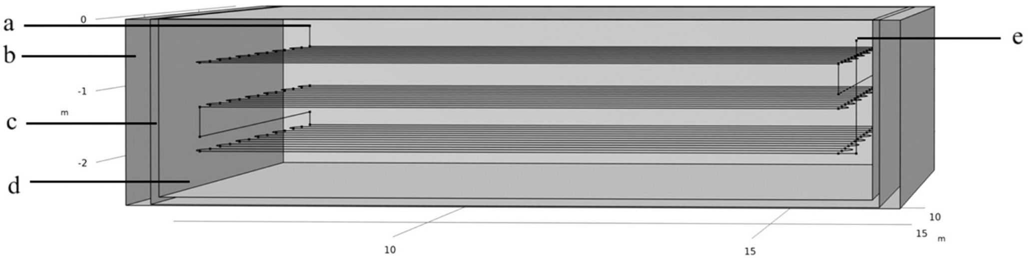

Fig. 6. Geometric model of the TES: a – inlet of the pipe, b – foundation, c – thermal insulation, d – sand domain, and e – outlet of the pipe.

model.

ue_t – The tangential velocity [m/s].

d_h – The inner pipe diameter [m], following the DN20 copper characteristics.

To further evaluate the thermal performance, a charging efficiency analysis was performed to quantify how effectively the stored energy was retained under different circulation strategies using the following Eq. (12):

$$Q_{stored/lost} = \frac{m_{soil}c_{p,soil}}{V}\int_0^V (T((x,y,z),t_{end}) - T((x,y,z),t_{start}))dV. \tag{12}$$

Where:

$Q_{stored/lost}$ – The net thermal energy stored in the sand or lost from the sand [J].

m_{soil} – Mass of the sand [kg].

$c_{p,\ soil}$ – Specific heat capacity of the sand [J/kg.K].

V – Total volume of TES sand domain [m^3].

$T((x,y,z),t)$ – Temperature at spatial position (x,y,z) and time t [s].

t_{start} and t_{end} – The period of simulation starts from 0 s to 604800 s.

The governing equations were spatially discretized using the finite element method (FEM). Transient simulations were carried out using COMSOL's time-dependent solver employing an implicit backward differentiation formula (BDF) scheme with adaptive time stepping. The nonlinear coupling between the pipe flow and the surrounding solid domain was resolved using COMSOL's built-in Newton-based solver, and the resulting linear system was solved using the sparse direct solver (PARDISO). Mesh refinement and time step sensitivity analyses were conducted, and further refinement produced negligible variations in predicted temperature fields, confirming numerical stability and solution independence.

4. Experimental results

The experimental study investigated the thermal performance of a thermal energy storage system by analysing thermal charging, heat dissipation, and the soil's heat accumulation. The system received a controlled heat input of 690 W for two hours daily over eight days. Soil temperatures were monitored at heights of 0, 0.1, 0.5, 0.9, and 1.0 m, with initial values of 5.5, 5.4, 4.6, 3.1, and 2.8 ℃, respectively. The change in temperature at each depth during the first 24 h is shown in Fig. 7. The numerical results presented here from COMSOL were evaluated alongside the measured temperature profile within this section.

Upon activation, the heating tubes and steel surface initially absorbed most of the input energy, delaying soil heating. A measurable temperature rise at the surface ($d = 0$ m) to 6.1 ℃ occurred at $t = 46$ s, indicating the onset of conductive heat transfer. Rapid surface heating followed as the steel surface heated, reaching 15.0 ℃C at $t = 444$ s, and 50.0 ℃ by $t = 3589$ s. According to the results shown in Fig. 8, the average heat flux density during the first hour peaked at $q_{avg,h} = 1503$ W/m^2, driven by a high thermal gradient.

In the second hour ($t = 7199$ s), the surface temperature reached 72.9 ℃, with the lower heat flux density of $q_{avg,h} = 684$ W/m^2, reflecting reduced thermal gradients and increased energy dissipation to deeper layers.

When storing heat in the ground, the soil layer directly in contact with the heating device is the first to heat up. In the case of a flat heated surface at the bottom of the accumulator, the soil above it is warmed initially, and over time, heat transfers upward to more distant layers. The heat flux density was less there due to heat storage in previous layers and loss to the environment.

After two hours, the heating device was turned off, initiating a sharp drop in temperature at $d = 0$ m. The soil temperature of this layer had decreased to $T_0 = 50.1$ ℃ during the next hour, with an average heat flux of $q_{avg,h} = 235.8$ W/m^2. Over time, the heat transfer rate declined further, and by $t = 25{,}196$ s, the temperature dropped to $T_0 = 32.9$ ℃, with a reduced gradient and heat flux density of $q_{avg,h} = 4.8$ W/m^2. Between hours seven and fourteen, the temperature decrease slowed to $\Delta T_{avg,h}\ /\ t = 1.2$ °C/h, showing the system's approach toward equilibrium. By $t = 82{,}799$ s, the temperature stabilised approximately at $T_0 = 19.7$ ℃.

At $d = 0.1$ m, the first temperature rise ($T_{0.1} = 6.0$ °C) occurred at $t = 974$ s, delayed by 926 s relative to $d = 0$ m, due to thermal resistance (Fig. 7). The heat transfer was driven by the strong gradient (grad$T = (T_0 - T_{0.1})\ /\ l_{0-0.1} = 173$ °C/m) and increased steadily. By $t = 3585$ s, $T_{0.1} = 14.9$ °C, the heat flux density peaked at $q_{avg,h} = 335.2$ W/m^2 (Fig. 8). The maximum temperature of $T_{0.1} = 36.1$ °C was reached at $t = 10{,}308$ s, after the heating device had turned off, showing delayed heat transfer. Thereafter, temperature decline was gradual, with $\Delta T_{\text{avg,h}}\ /\ t = 1.4$ °C/h over the next three hours and reduced conduction from the soil layer at $d = 0$ m ($q_{avg,h} = 58.3$ W/m^2). Later, dissipation slowed further, and by $t = 82{,}799$ s, the temperature stabilised at $T_{0.1} = 19.7$ °C.

At the more distant layers (Fig. 7), heat transfer was more gradual. At $d = 0.5$ m, a temperature increase was first recorded around the fourth

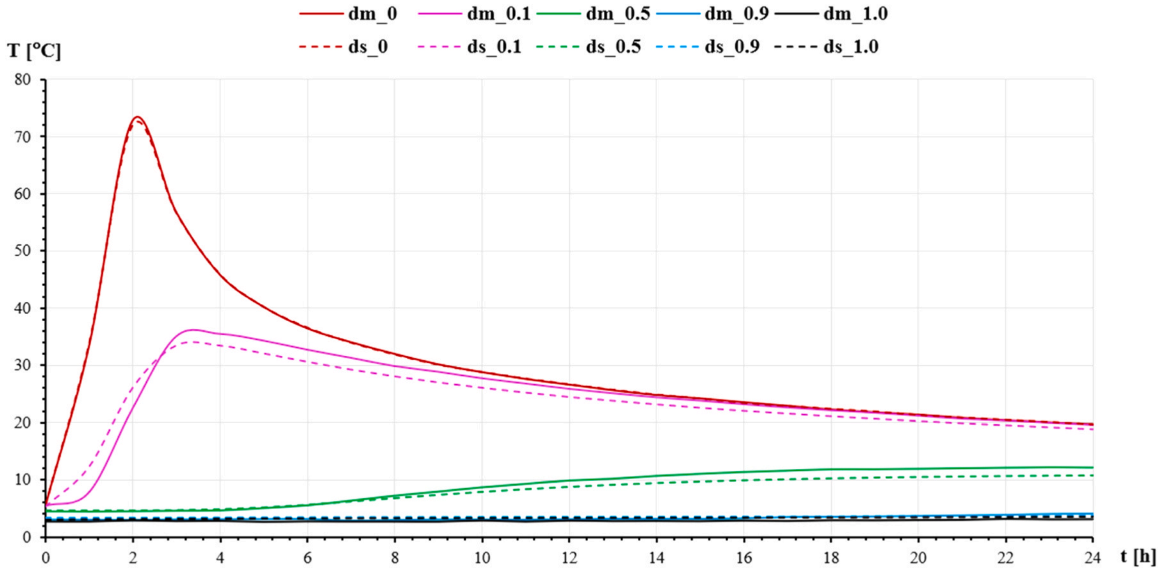

Fig. 7. Measured (d_{m}) and simulated by COMSOL (ds) temperature profiles at various distances for two hours of charging during one day.

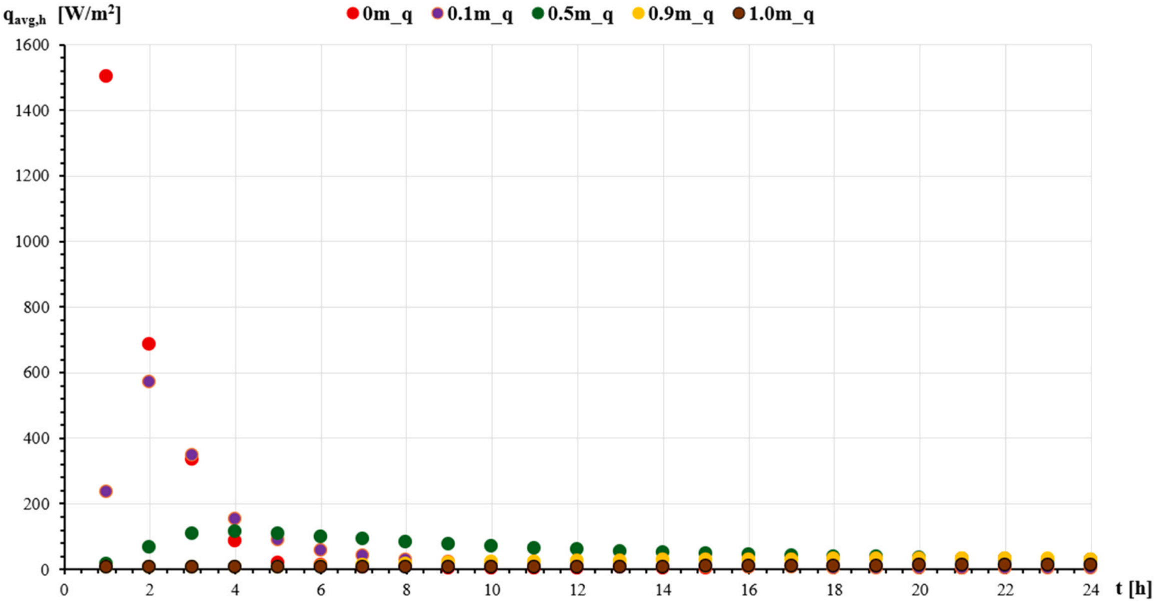

Fig. 8. Change in the average hourly heat flux density at various distances for twenty-four hours.

hour, reaching $T_{0.5}$ = 4.8 ℃. The initial sharp temperature gradient between 0.1 m and 0.5 m, calculated as (($T_{0.1} - T_{0.5}$) / $l_{0.1-0.5}$ = 79.0 °C/m), induced a rapid increase in conductive heat flux at this depth. This was reflected in the hourly average heat flux, which rose sharply from $q_{avg,h}$ = 15 W/m^2 in the first hour to a peak of $q_{avg,h}$ = 112.3 W/m^2 at the fourth hour. As the temperature gradient began to diminish, the flux gradually decreased, indicating a deceleration in thermal conduction. By the twelfth hour, $T_{0.5}$ had increased to 10.1 °C, with the flux dropping to $q_{avg,h}$ = 58.5 W/m^2. Eventually, by t = 75,540 s, the temperature stabilized at 12.2 °C, while the heat flux fell below qavg,h = 30 W/m^2, marking the transition to near equilibrium.

Heat propagation at d = 0.9 m and d = 1.0 m was significantly slower, with thermal response delayed due to reduced gradients. At 0.9 m, a noticeable temperature increase began after the eighth hour, driven by a gradient of (($T_{0.5} - T_{0.9}$)/$l_{0.5-0.9}$ = 11.3 ℃/m) from the 0.5 m layer. Corresponding average heat flux gradually rose from $q_{avg,h}$ = 5.1 W/m^2 to $q_{avg,h}$ = 29.0 W/m^2 by the twenty-fourth hour, while temperature reached $T_{0.9}$ = 4.1 ℃ by the twenty-second hour. At 1.0 m, temperature rise was minimal ($T_{1.0}$ = 3.2 °C by t = 79,197), sand heat flux remained consistently low, increasing only from $q_{avg,h}$ = 4.8 W/m^2 to $q_{avg,h}$ = 12.8 W/m^2 over twenty-four hours. These deeper layers primarily acted as thermal buffers, enabling gradual energy accumulation with minimal short-term dissipation.

Day after day, during the two-hour thermal charging period, the temperature of the TES's sand filling continues to rise. In practice, this means that each successive charging cycle begins from a higher baseline temperature. Depending on the type of charging device used, this can influence the duration, intensity, and overall efficiency of the charge. The observed charging and discharging patterns for twenty-four hours provide insights into the short-term thermal response of the soil. However, to understand the progressive accumulation and retention of heat, it is essential to examine the variations in temperature over an extended period. Repeated charging cycles over eight consecutive days (Fig. 9) allowed heat to propagate deeper into the soil, revealing how thermal energy is absorbed and retained at various depths.

A detailed analysis of the temperature increase at different points indicated varying thermal responses within the TES. On day one, the temperature of the soil in contact with the heating surface (d = 0 m) rose

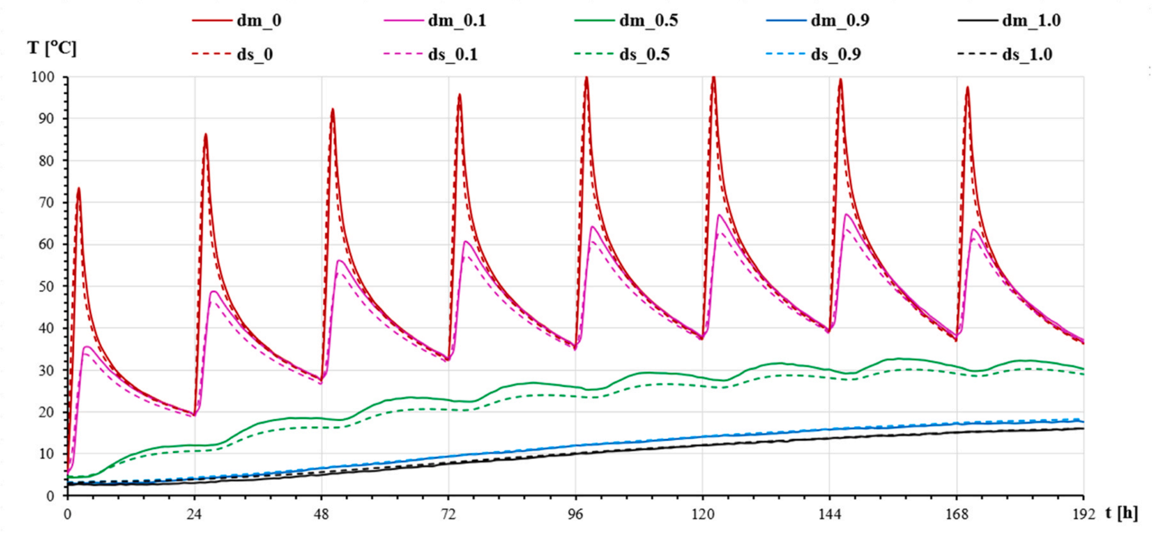

Fig. 9. Comparison of measured and simulated temperatures by COMSOL over eight days at d = 0, 0.1, 0.5, 0.9, and 1.0 m.

by $\Delta T_0 = 13.9$ ℃, while at $d = 0.1$ m by $\Delta T_{0.1} = 14.1$ ℃ – representing the layers with the highest heat gain. In contrast, distanced soil layers showed a minor increase in temperature: 7.5 ℃ at $d = 0.5$ m, 1.0 ℃ at $d = 0.9$ m, and 0.5 ℃ at $d = 1.0$ m. This indicates a steep thermal gradient and concentrated heat retention near the surface. By the second day, the soil layers at $d = 0$ m and $d = 0.1$ m continued warming but at a slower rate of temperature: 8.2 ℃ and 8.1 ℃. Day three showed distribution, with distanced layers $d = 0.5$ m, 0.9 m, and 1.0 m absorbing more heat. There, the temperature increased by 4.4 ℃, 2.8 ℃, and 2.6 ℃, respectively, although the rate of surface warming declined (Fig. 9).

The temperature profile becomes more uniform on the sixth and seventh days. Over eight consecutive days (Fig. 9), this cumulative effect resulted in a sustained temperature rise across all depths, with the strongest response from the layers near the heating device and an increasing storage contribution from the distant layers daily.

The experimental setup, installed in the ground and insulated from external influences, provided a controlled representation of the local thermal behaviour around a heated surface in soil. This short-term field experiment captured how heat spreads vertically through moist sand, revealed depth-dependent temperature delays, and quantified realistic heat flux levels under subsurface conditions. These measured responses informed the development of the numerical model, which incorporated the same material properties, heat-input regime, and the conduction-dominated heat-transfer mechanism in COMSOL Multiphysics (v6.1). An identical TES geometry was recreated in the simulation to replicate the experimental setup (Fig. 2) and conditions, and allow direct comparison. Tracking temperatures at corresponding depths confirmed that the model reproduced the experimentally observed thermal gradients, upward heat propagation, and daily charging behaviour. The maximum deviation between the measured and simulated temperature was 8% at d $= 0.5$ m (Fig. 9), demonstrating that the model reliably captures transient heat transfer in the sand. The experimental campaign is intended to validate the governing transient heat transfer behaviour and provide confidence in material and model parameters, rather than to directly represent full-scale seasonal start-up performance. With this validation, the numerical simulation was then extended to represent the full-scale 300 m^3 TES volume, embedded pipe networks, and multi-day solar-charging regime, generalizing the experimentally verified behaviour to realistic operational conditions.

5. Numerical simulation results

To comprehensively assess the thermal performance of the TES system coupled with a solar thermal collector, numerical simulations were carried out over a week, starting on June 21st, the summer solstice, which represents the peak of solar radiation in Kaunas, Lithuania. Two cases were examined to understand the influence of initial storage conditions. In the first case, the TES was assumed to be empty at the start of the simulation week, representing a baseline charging scenario. In the second case, the TES was partially charged from earlier solar input before June 21st, reflecting more realistic operating conditions. The fluid circulated at a constant flow rate of 288 l/h, and the inlet temperature applied to the TES (equal to the outlet temperature from the solar thermal collector, $T_{fl,coll,out} = T_{fl,in} = T_{inlet}$) was defined as a time-dependent boundary condition.

In both cases, simulations were conducted for the same week of charging. The daily thermal energy input for the empty TES scenario averaged approximately 54.7 kWh per day. The first day of the simulation, during which 55.1 kWh (Eq. (8)) of thermal energy was supplied, was selected for detailed analysis to evaluate the system's transient thermal response. The full-week results were used to assess cumulative heat storage and the impact of pre-charging. These boundary profiles were implemented in COMSOL Multiphysics, where transient heat transfer simulations were performed to investigate the spatial and temporal temperature evolution within the TES domain.

The average monthly air temperature in Kaunas in June is $T_{air} = 16.3$ ℃ (“Technical Regulations for Construction, STR 2.01.02:2016, Energy Performance Design and Certification of Buildings”, 2025). This value was used in the simulation, assuming a constant temperature throughout the day. The TES operating simulation began at midnight ($t = 0$ s) with an inlet temperature of $T_{inlet} = T_{air}$, representing the temperature of the fluid outflowing from the solar collector (Fig. 10). The initial average sand temperature was approximately $T_{avg,sand} = 13.3$ ℃, close to the average typical ground temperature in June in Kaunas, Lithuania, starting from 0 to −2.5 m depth. Typically, during the night, with decreased air temperature, the circulation of the liquid in the collector circuit is stopped to prevent heat loss to the atmosphere. However, since the air temperature is higher than the ground temperature, the circulation can be left unstopped with a small thermal load on the TES (Fig. 11).

As the day progressed and solar radiation increased, the outlet temperature of the solar thermal collector rose accordingly, resulting in a gradual rise in the TES inlet temperature. At $t = 28{,}800$ s, the fluid entered the system at $T_{inlet} = 24.1$ ℃, with an outlet temperature of $T_{outlet} = 12.2$ ℃ and an average sand temperature around $T_{avg,sand} = 13.4$ ℃. The heat transfer rate exceeded $Q_{transfer} = 3251$ W. The value of the outflowing fluid temperature (T_{outlet}) was lower than that of the TES average soil temperature ($T_{avg,sand}$) due to the soil temperature distribution in dependence on the depth and the position of the pipes of the loops near the outlet position (Fig. 6). As the sun moved toward its zenith, the thermal output from the collector increased steadily, further raising the inlet temperature. By $t = 36{,}000$ s, the T_{inlet}, T_{outlet}, and $T_{avg,sand}$ reached 30.5 °C, 13.0 °C, and 13.5 °C, respectively, while the heat transfer rate climbed above $Q_{transfer} = 4797$ W. The maximum rate of heat transfer to the soil was observed at $t = 46{,}800$ s, where $Q_{transfer} = 6169$ W was recorded, driven by a peak temperature difference of 22.4 °C ($\Delta T_{max} = T_{inlet} - T_{outlet}$). This moment corresponds to the time when the sun was at its highest position in the sky, and the solar thermal collector was operating at maximum output. As a result, the inlet temperature to the TES reached its peak, significantly enhancing the heat input to the system and accelerating thermal accumulation in the sand layers surrounding the heat exchanger pipes.

As the energy input continued, the near-pipe soil layers became progressively warmer. Due to the relatively slow heat transfer process, the temperature difference between the fluid and the surrounding soil began to decrease. The gradual reduction in heat transfer at the inlet zone of the TES meant that the fluid maintained a higher temperature and carried heat to other areas and a greater depth within the TES (Fig. 6). These interactions are reflected in the temperature field in Fig. 11.

In the evening hours, solar radiation declined, and the inlet fluid temperature dropped; the temperature gradient between the fluid and the near-soil layers, which the day’s heat input had warmed, gradually diminished, resulting in a reduced heat transfer rate. Throughout the first twenty-four hours, however, energy continued to flow from the warmer fluid to cooler soil, and no reversal in heat direction was observed. Throughout the week, repeated charging cycles led to a steady rise in TES average temperature $T_{avg,\ sand}$, from 13.3 °C to 16.2 °C, reflecting a cumulative increase of about 0.4 °C per day in the initially uncharged soil domain.

The reversal in the heat transfer direction occurred only later in the simulation, around $t = 598{,}000$ s on the seventh day (Fig. 10), when sustained daily charging raised the near-pipe soil layer temperatures above those of the evening fluid. At that point, heat began to transfer from the TES back into the fluid ($Q_{transfer} < 0$), highlighting the need for flow control to prevent unnecessary energy loss, which is further examined in the following section.

In the second simulation scenario, the TES was assumed to be partially charged at the start of the one-week evaluation period, representing the accumulation of solar thermal energy during spring and early summer. As described in 3.1, the cumulative solar irradiance on a surface tilted at 40 ° from May 1st to June 21st totalled approximately

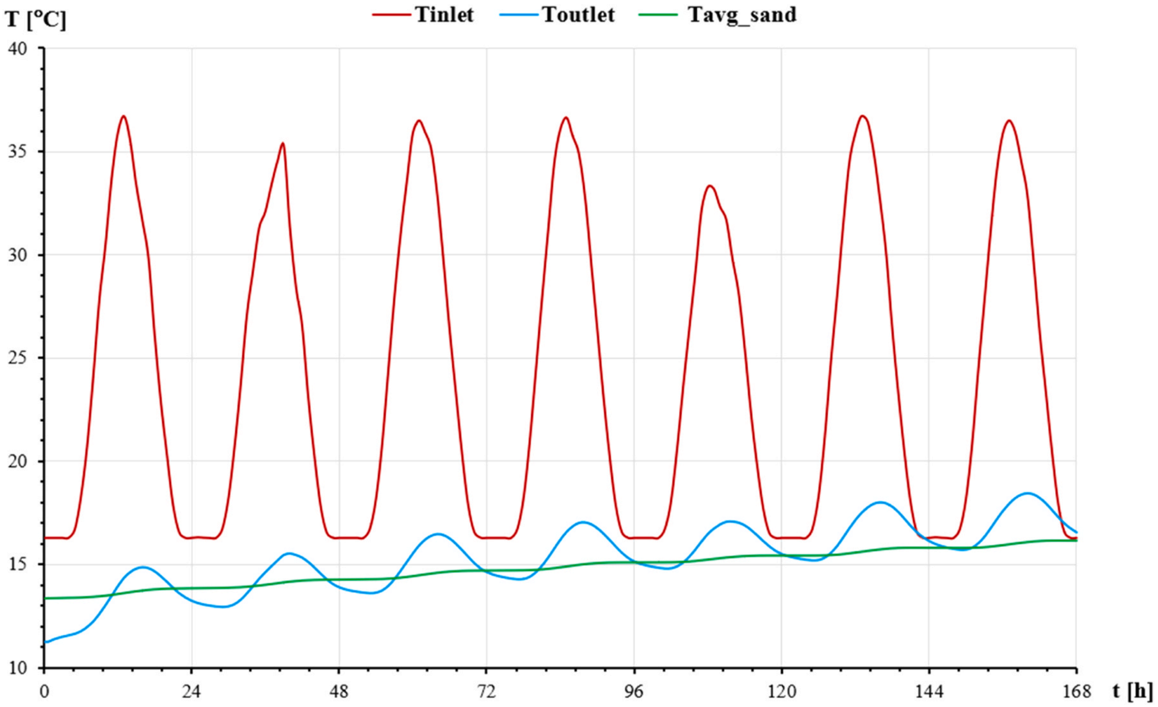

Fig. 10. The change in the energy storage's inlet and outlet fluid and average sand temperatures over seven days, computed by COMSOL Multiphysics.

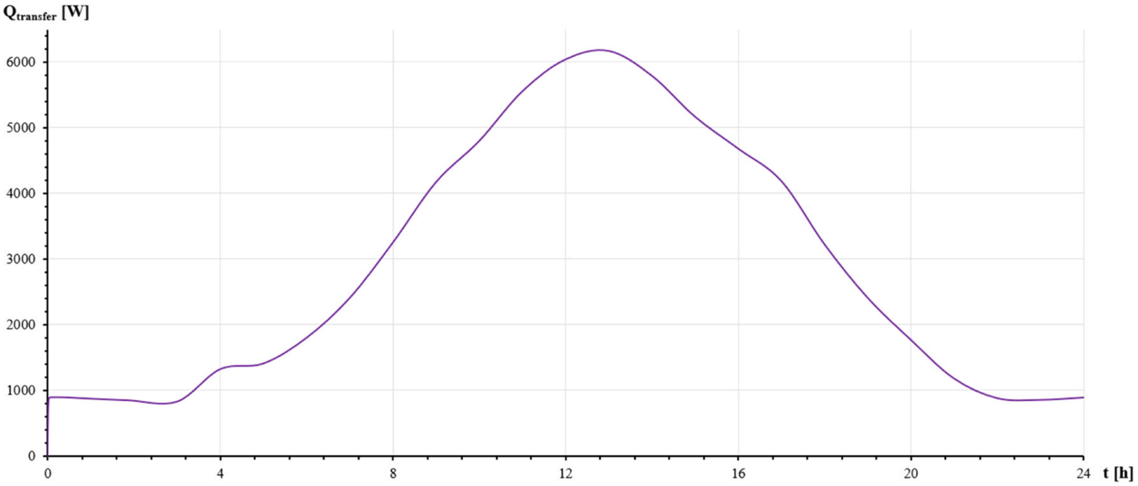

Fig. 11. Heat transfer from the fluid to the energy storage's soil over the first twenty-four hours, computed by COMSOL Multiphysics.

953.5 MJ/m^2, based on monthly and partial-month values. The corresponding initial average temperature of sand in TES was calculated using Eq. (8), which relates the stored thermal energy to mass, specific heat capacity, and temperature increase of the storage medium.

To improve efficiency and prevent energy losses to the atmosphere, a flow-controlled strategy was implemented: fluid circulation was enabled only when the temperature of the fluid, which outflowed from solar collectors and entered TES ($T_{fl,coll,out}$=T_{inlet}), exceeded the average TES sand temperature ($T_{avg,sand}$). Once this condition was met, the circulation pump was turned on, and fluid circulation began (activated system meant "1"). Circulation was stopped when the inlet temperature (T_{inlet}) became less than or equal to the average sand temperature in TES: $T_{inlet} \leq T_{avg,sand}$ (deactivated system meant "0") (Fig. 13).

Due to the high inertia of the charged heat dissipation in the full volume of the TES, the distribution of the sand's temperature was visible within the TES (Fig. 14). A daily increase in the average soil temperature of the TES was observed when analysing the operation of the soil-type thermo-accumulator over a week (Fig. 13). This required the solar collector fluid to be heated to a higher temperature before activating circulation after each night. On the other hand, the circulation had to be stopped earlier in the evening to avoid heat loss to the atmosphere. Therefore, a slight reduction in system activation intervals was observed over the course of a week.

In the case of an operating TES, it is partially charged with heat. This means that at night, the average temperature of the soil in TES and the temperature of the fluid outflowing from TES are higher than that of the atmospheric air. At night, the collectors do not generate heat. A portion of the heat would be lost to the atmosphere while the fluid of higher temperature flows through them. For this purpose, as mentioned, the disconnection of the fluid circulation was simulated during the dark period. However, it is necessary to determine the moment at which circulation needs to be started. During the night, the temperature of the

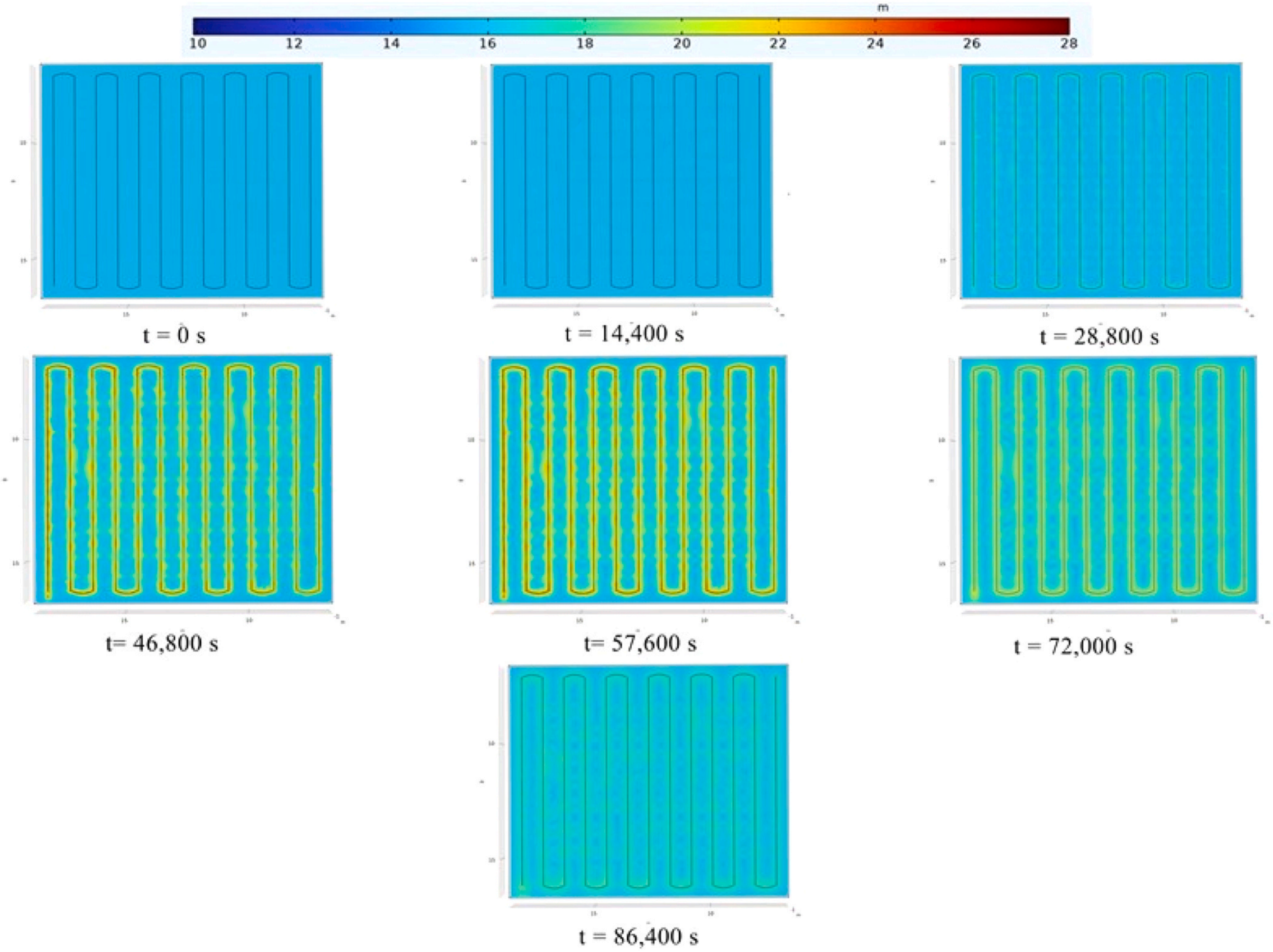

t = 0 s

t = 14,400 s

t = 28,800 s

t= 46,800 s

t= 57,600 s

t = 72,000 s

t = 86,400 s

Fig. 12. Temperature distribution of the first layer in the TES system at different time steps, ranging from 0 h to 24 h on the first day of the week, illustrating heat propagation from the pipe network into the surrounding soil, as computed by COMSOL Multiphysics.

fluid in the collector area reaches the atmospheric temperature due to heat losses. The decision was made to initiate fluid circulation when the fluid is heated by solar radiation to a temperature equal to or by 2–4 ℃ higher than the average sand temperature in the TES ($T_{avg,sand}$).

With daily charging of the TES and rising $T_{avg,sand}$, more time will be needed to heat the fluid in the collectors each morning. The circulation will be turned on later. On the other hand, due to the higher soil temperature, as the intensity of solar radiation decreases in the evening, the circulation will have to be stopped earlier. As a result, with the same intensity of solar radiation, the daily TES loading time will be shorter. This means that the actual TES loading time will be shorter than the calculated one when the TES charging degree (TES soil temperature) is not considered.

The amount of fluid in the circulating system of collectors may vary from 10 to 25 litres, depending on the type of collectors, their connections, the connection of heating pipes, and other factors. During the study, 12 litres of fluid were present in the heating system of the collector area. After stopping the fluid circulation in the system, due to heat losses to the environment, the fluid temperature was equal to the ambient air temperature (T_{air}) in the morning, before sunrise. Therefore, the energy of the incoming solar radiation was initially used to heat the fluid to the average soil temperature of the TES ($T_{avg,soil}$). The amount of heat consumed to heat the fluid was calculated by the formula (Eq. 13):

$$E_{coll} = V_{fl,coll}\rho_{fl}c_{p,fl}\left(T_{avg,sand,t(i)} - T_{air,t(i)}\right). \tag{13}$$

Where:

E_{coll} – thermal energy, to heat the fluid of the circulation system, located in the collector circuit, to a temperature equal to $T_{fl,coll,out(i)} = T_{avg,sand,t(i)}$ [J].

$T_{avg,sand,t(i)}$ – TES soil temperature, at current time moment: $t = i$ [℃].

$T_{air,t(i)}$ – atmospheric air temperature, at current time moment: $t = i$ [℃]. It was assumed to be equal to the average daily temperature in June.

An average monthly value of the air temperature in June near Kaunas was used for calculations: $T_{air,t(i)}= 16.3$ ℃. In real conditions, the night air temperature varies from 15 to 10 ℃, and in the morning, the temperature is lower (near 10÷12 ℃). In the second simulation case, $T_{avg,sand,t(i)}$ was initially set to 30 ℃. This meant that the amount of energy equal to $E_{coll}= 612$ kJ (0.17 kWh) was required for fluid heating to initiate circulation. At early morning, on the 21st of June, the solar radiation $P_{sol,rad}$ increased from $P_{sol,rad}\approx 0$ at $t = 4{:}30$ to $P_{sol,rad}= 13.18$ W/m^2 at $t = 5{:}00$, to $P_{sol,rad}= 30.74$ W/m^2 at $t = 5{:}30$, and to $P_{sol,rad}= 61.49$ W/m^2 at $t = 6{:}00$ ("Kaunas June Weather, Average Temperature Lithuania - Weather Spark.", 2025). Accordingly, the power of collectors increased from $P_{coll}\approx 0$ at $t = 4{:}30$ to $P_{coll}= 126$ W at $t = 5{:}00$, to $P_{coll}= 279$ W at $t = 5{:}30$, and to $P_{coll}= 587$ W at $t = 6{:}00$ (Fig. 15). Here, the assumption was made that the collectors themselves do not need to be heated, and their efficiency remains constant and equal to $\eta_{coll}= 0.53$. Therefore, the time to heat the fluid was $t = 4067$ s ($t = E_{coll}/P_{coll}$).

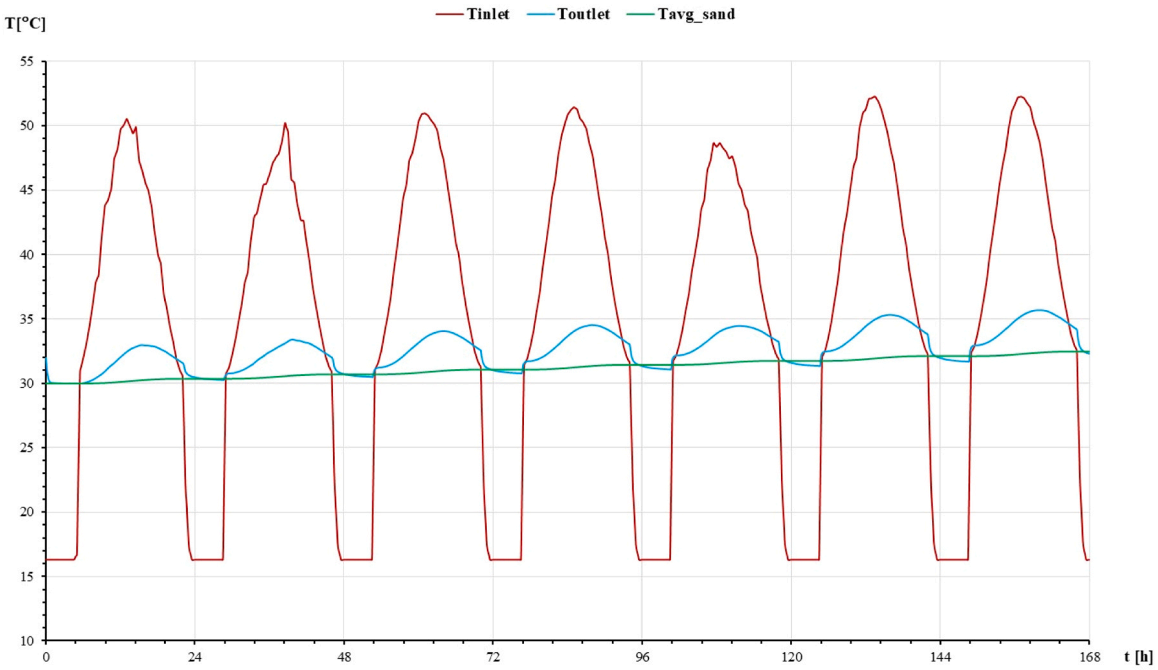

Fig. 13. The change in the energy storage's inlet and outlet fluid over a seven-day cycle for controlled flow of partially charged TES, computed by COMSOL Multiphysics.

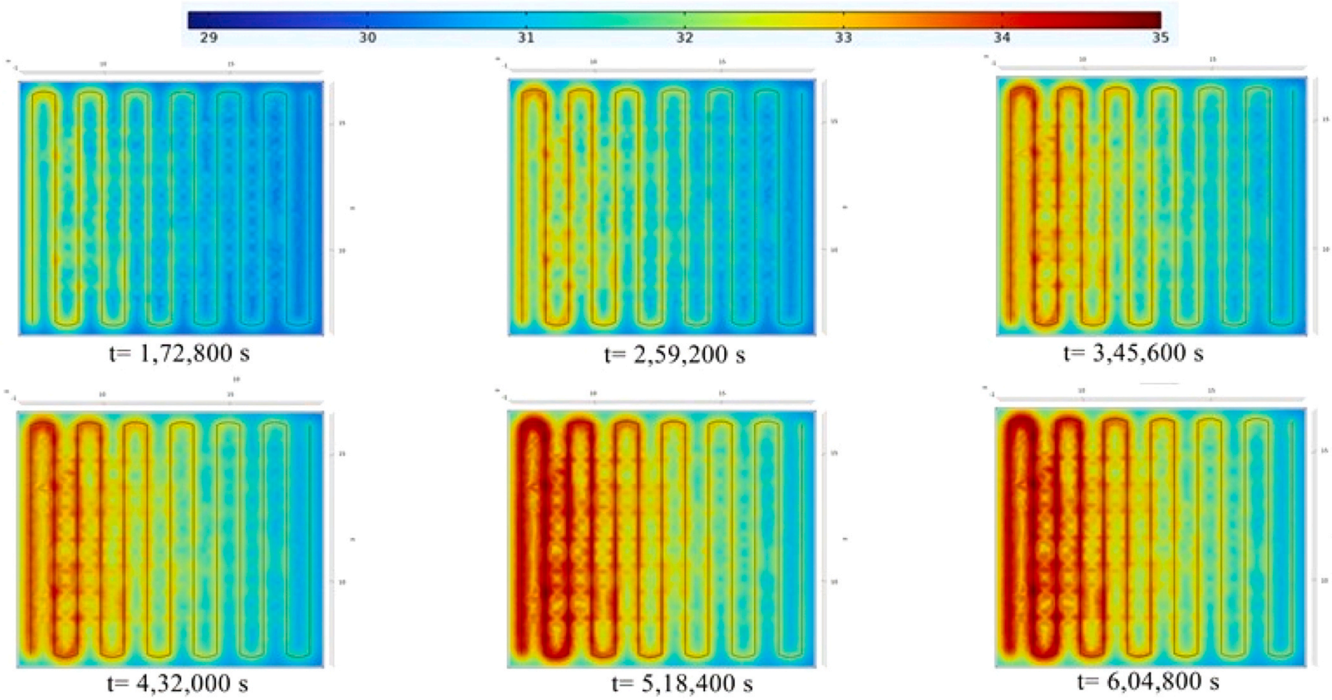

t= 1,72,800 s
t= 2,59,200 s
t= 3,45,600 s
t= 4,32,000 s
t= 5,18,400 s
t= 6,04,800 s

Fig. 14. Temperature distribution of the first layer in the partially charged TES system at different time steps, showing heat propagation from the pipe network into the surrounding soil from the second day (t = 1,72,800 s) to the seventh day (t = 6,04,800 s) with a one-day interval, under controlled flow.

The system will remain warmed by turning off the fluid circulation in the evening. Therefore, at nighttime, a similar amount of energy will be dissipated as heat losses in the atmosphere. On June 21, during the day, about 53.2 ± 4.1 kWh of energy is generated in the collectors. When $T_{avg,sand,t(i)} - T_{air,t(i)} = 13.7$ ℃, the energy losses (2 ×0.17 kWh) due to the shorter charging time interval reach only 0.64 per cent. However, the best condition for heat generation and TES charging with heat was analysed.

In the case of a more charged heat storage system: $T_{avg,sand,t(i)}$= 35 ℃, and more cold nights: $T_{air,t(i)} \approx 10$ ℃, a higher amount of energy is needed to heat the fluid: E_{coll}= 1117 kJ (0.31 kWh). The loss in energy is 1.17 per cent for this case (Fig. 15). It should also be noted that the charging time of the thermal storage system significantly shortens as well: $\Delta t = 5271–4067 = 1204$ s. It means a bit more than 20 min in the morning.

Using real operating conditions of solar collectors for simulation, the

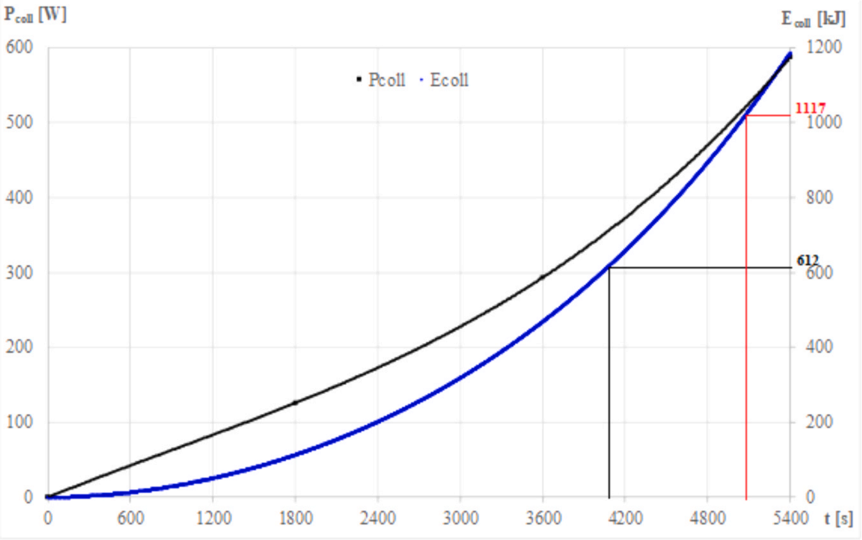

Fig. 15. The loss in heat to start the heat storage system charge process at early morning (4:30 AM), on the 21st of June, near Kaunas.

daily TES charging intensity varied according to changes in cloudiness, air temperature, and other factors. This has a direct impact on the TES charging time interval, not only on the same day, but also on subsequent days. Higher TES charge losses due to the reduced time interval occur in September when the temperature difference $T_{avg,sand,t(i)} - T_{air,t(i)}$ increases to 50 °C. At this time, the intensity of solar radiation is significantly lower, and the weather is more cloudy and rainy. The aforementioned energy losses may even approach the 5 % limit.

6. Discussion

The experiment provided insights into the performance of the soil-based thermal energy storage system under controlled conditions with minimal daily temperature variations (Chapter 4). The two-hour daily heating period represented intermittent energy input, allowing for the observation of short-term heat storage without overheating. The eight-day experiments captured heating (charging) and cooling (discharging) cycles, avoiding seasonal shifts. The electric heating device in the experimental setup delivered a study and concentrated thermal input over a small surface area, creating a strong local temperature gradient in the sand. This was intentional, as it mimicked the localized heat transfer conditions that occur around the heat exchanger pipes during solar-assisted charging. In the numerical model, the thermal energy supplied by the solar collectors was distributed along the entire pipe network, producing a lower but more uniform heat flux into the surrounding sand. Although the intensity and distribution of the heat differ between the two configurations, both systems rely on conduction as the dominant heat-transfer mechanism within the sand. As a result, the experimental setup accurately captures the local thermal behaviour of the sand near a heat source, making it directly relevant for validating the numerical model developed for the full-scale storage system. This ensures consistency with the established heat-transfer similarity principles for conduction-controlled systems (Bergman et al., 2011).

Precipitation and groundwater influences were not considered because the TES was covered with polyethene, which prevented water infiltration and ensured consistent boundary conditions (Chapter 4). The sand used in the TES contained approximately 10% moisture, representing an average gravimetric water content for compacted sandy soils in Kaunas at shallow depths. Field data from Lithuanian sandy deposits indicate typical unsaturated moisture content of about 4–9% and up to 14–23% when saturated, while general spoil-physics datasets report field capacities of 6–10% gravimetric for sand. Thus, 10% was adopted as a representative mid-range value corresponding to realistic locval summer conditions while avoiding both dry and near-saturated extremes (Allen et al., 2006; Dundulis et al., 2006). Because the experimental setup was sealed with polyethylene, the moisture content did not change during the eight-day test, and no evaporation or infiltration occurred. Therefore, transient moisture migration and its effect on thermal conductivity were not relevant under these controlled conditions, and a fixed moisture was appropriate for both the experimental interpretation and the numerical model. Nevertheless, moisture-dependent thermal conductivity is an important factor in natural, unsealed soil systems and represents a valuable direction for future investigation (Chapter 2).

The analytical approach assumed that the temperature remains below 100 °C and is discharged naturally, with significant heat loss through the walls of the TES to the surrounding ground. However, it is important to note that the heat lost to the sides and the bottom may have acted as secondary heat sinks, though this aspect was not investigated in this study and remains an area for future exploration. The shallow placement of the TES (0.1 m below the ground surface) exposed it to near-surface temperature changes. While deeper placement could stabilise temperatures, the chosen depth provided insight into the performance of shallow burial conditions (Chapter 4).

The observed delay in temperature rise at deeper layers was attributed to the soil's thermal inertia and time lag associated with heat conduction (Chapter 4). As the heat propagates upward (away from the heating source in this case), deeper layers take longer to respond due to the gradual nature of conductive heat transfer. This is influenced by the soil's ability to store and slowly release heat. However, this study did not quantify the specific impact of increasing depth on the time lag.

Mesh refinement and time step sensitivity checks were performed to confirm numerical robustness. Further mesh refinement and reducing the time step produced negligible changes in temperature results, confirming that the model is mesh-independent and time-step independent (chapter 4). The numerical study (Chapter 5) effectively implemented controlled flow conditions, ensuring that circulation occurred only when a favourable temperature gradient was present, i.e., a fluid temperature higher than the soil temperature. During periods with no solar radiation (i.e., nighttime), the solar input was set to zero, and the outlet fluid temperature was assumed equal to the ambient air temperature for the respective hours. This assumption allowed for a simplified yet conservative representation of system behaviour during non-active hours and supported the logic of surpassing circulation when thermal charging is not viable. The pipe layout and positioning also play a critical role in heat distribution within the TES system. Pipe arrangements that maximise surface contact and promote uniform fluid-solid interaction can significantly influence localised temperature gradients and overall system efficiency. However, more advanced adaptive flow mechanisms were not explored, such as varying flow rates based on real-time temperature gradients across different soil depths. And the adopted internal heat transfer coefficient $h_1 = 70$ W/(m^{2}K) is consistent with laminar internal flow, as the Reynolds number computed using the standard relation for flow in circular pipes was 1751, which is below the laminar-flow threshold of 2300 and therefore justifies the use of laminar-flow Nusselt correlations (Bergman et al., 2011) (chapter 3). While the schematic used in the numerical model includes a heating system to illustrate the possible integration with building thermal loads, this component was not included in the present simulations. The focus remained solely on transferring thermal energy from the solar collector to the TES.

In the present systems, auxiliary energy consumption is mainly associated with the circulation of the heat transfer fluid through the TES piping network. Hydrauklix assessment using the actual pipe length (390 m), the inner diametr (0.02 m), and the flow rate (288 L/h) indicates laminar flow Re = 1751) with a frictional pressure drop of approximately 0.24 bar (2.36 m head), corrsponding to a hydraulic power of about 1.91 W (4–8 W, electrical with realistic efficincies). This estimate is consistent with the practical operation of commercial circulation pumps, for example, a Wilo-Yonos PICO 15/1–4 (H_max = 4.3 m, Q_max = 2.7 m^3/h) specifies an electrical input of 4–20 W, and would operate near the lower range (4–8 W) at the present low-flow, low-head conditions. Compared to the kilowatt-level thermal charging power and seasonal energy input in the MWh range, this auxiliary demand is negligible (below 1%) and was therefore not explicitly included in the analytical thermal performance calculation (“Yonos PICO 15/1–4, Wilo.”,2026).

In addition, compared to conventional Borehole Thermal Energy Storage (BTES), the soil-based TES system showed several key advantages. First, it eliminates the need for deep drilling and specialized borehole equipment, reducing installation cost by up to 40–60%, as drilling alone can account for up to 45% of total BTES investments depending on site conditions (Gao et al., 2023). Second, its shallow placement allows for easier integration beneath buildings and direct coupling with solar thermal systems. Third, heat is stored and transferred directly within the sand, avoiding the thermal resistance found in BTES. Finally, the simpler design minimises long-term maintenance risk, such as fluid leakage or borehole degradation, making it a suitable option for compact building-level energy storage.

7. Limitations and future work

The present study was designed to experimentally validate and numerically analyse the short-term thermal behaviour of a sand-based thermal energy storage system under empty, partially charged, and controlled charging-duration conditions. While the eight-day experimental campaign provided robust insight into near-field conductive heat transfer, temperature propagation within the storage medium, and transient response at multiple depths, it does not directly represent seasonal-scale charging and discharging behaviour or long-term thermal stabilization of the surrounding soil. Full seasonal operation involves significantly longer timescales, boundary self-conditioning, and cumulative heat-loss dynamics that require extended experimental monitoring or multi-cycle numerical simulation.

To ensure controlled and repeatable conditions, moisture migration and groundwater interaction were intentionally excluded by sealing the storage volume with polyethylene insulation layers. This approach allowed isolation of pure conductive heat transfer within the sand medium; however, real ground-based storage systems may experience coupled heat-moisture transport, evaporation-condensation processes, and moisture-dependent variations in thermal conductivity. Consequently, the present results primarily represent dry or hydraulically isolated storage conditions and should be interpreted accordingly when extrapolating to unsealed field installations.

Heat dissipation through the lateral and bottom boundaries of the storage volume was acknowledged as a major loss pathway, yet the present analysis did not explicitly decompose individual conductive loss contributions or quantify the transient buffering role of the surrounding soil. Furthermore, although the delayed temperature response observed at deeper measurement locations was attributed to thermal inertia and conduction-driven time lag, no parametric relationship between depth and response time was derived. Such relationships could improve simplified design-oriented models for compact seasonal storage systems.

The numerical simulations employed practical but simplified operational boundary assumptions, including zero solar input during non-irradiated periods and ambient air temperature representation for circulating fluid during inactive hours. While these assumptions provided conservative and computationally efficient conditions for evaluating charging behaviour, real collector loop dynamics and diurnal thermal inertia may alter short-term loss characteristics. Additionally, circulation control was based on a threshold temperature orientation, and more advanced adaptive control strategies were not explored within the present framework.

Future research should therefore extend the experimental and numerical framework to seasonal-scale operation, incorporate coupled heat-moisture transport under unsealed soil conditions, and explicitly quantify boundary heat-loss pathways. Integration of dynamic building loads and advanced control strategies, including variable flow operations such as circulation timing, intensity, and pipe design, and predictive scheduling based on solar availability, will enable full system-level assessment. In addition, parametric optimization of pipe layout, depth placement, and operational regimes should be conducted to enhance heat distribution uniformity and overall storage efficiency under realistic climatic conditions.

8. Conclusions

In cold-climate countries, a significant amount of heat is required for building heating in the winter. The thermal energy is obtained mainly by burning fossil fuels, whether the building uses an autonomous heating system or is connected to the district heating network. Solar collectors are often used to produce hot water, particularly during warmer periods. Heat storage systems would make it possible to use the heat accumulated in summer for the cold season. Using soil as a filler in thermo-accumulators is a cheap and straightforward option. The basement of the building or a limited volume of soil beneath the building can serve as the filler container. This research has shown that this is a promising solution for sustainable building heating, replacing fossil fuels with renewable energy sources, such as solar collectors.

The eight-day experiment revealed a pronounced depth-dependent thermal response within the oil-based storage. The layers located closest to the heating surface (0–0.1 m) showed the strongest cumulative rise, corresponding to a total gain of 30.8 °C at 0 m and 31.6 °C at 0.1 m. The slightly higher gain at 0.1 m demonstrates the natural thermal storage behaviour of soil, where a shallow subsurface layer accumulates and retains heat more uniformly than the immediate contact zone, which undergoes the fastest thermal cycling. The intermediate layer at 0.5 m observed a substantial amount of heat as well, achieving a cumulative gain of 26.1 °C. The layers positioned furthest from the heating surface exhibited a smaller initial increment but continued to rise progressively across all eight days, achieving gains of 14.3 °C at 0.9 m and 12.3 °C at 1.0 m by the eighth day. The most pronounced daily temperature increases occurred in the near-surface layers during the first charging cycles, 13.9 °C on day one and 8.2 °C on day 2, while the more distant layers showed slower but persistent heat accumulation, even on days seven and eight. Therefore, these results confirm clear functional stratification: rapid heat uptake in near-surface layers, moderate accumulation in the intermediate layer, and persistent long-term storage in the deeper layers.

Charging soil-type thermal energy storage systems by fluid heated in solar collectors has certain peculiarities. At night, the collectors do not generate heat, and a portion of the accumulated heat may be lost to the atmosphere when fluid at a higher temperature flows through them. Therefore, fluid circulation needs to be interrupted during the dark period. It was observed that the average soil temperature is more suitable for controlling circulation than the temperature of the fluid exiting the TES. The decision was suggested and discussed to initiate circulation when the fluid, heated by solar radiation, reaches a temperature equal to or 2–4 °C higher than the average soil temperature in the TES, and to stop circulation when the fluid temperature after collectors becomes lower than mentioned.

The charging of TES with heat begins from the initial soil temperature, which depends on the state of charge of the TES and is usually significantly higher than that of the atmospheric air. With daily charging, the soil temperature gradually increases, and each morning, additional time is required to heat the fluid in the collectors to the desired level. Due to the higher soil temperature, circulation also needs to be stopped earlier in the evening. This results in the actual TES loading time being shorter than the calculated one if the soil temperature is not taken into account. In such cases, higher-capacity equipment may be necessary to store the required annual amount of energy. Depending on the charge level, defined by the average soil temperature, the daily operating time of solar collectors for soil charging decreases, reducing the charging potential. In June, this reduction is less than one per cent, while in less favourable periods, such as September, it can reach about five per cent.

This research confirms that a compact, insulated soil-based TES system can serve as a cost-effective and adaptable solution for seasonal heat storage in buildings. By combining intelligent control strategies with a low-cost thermal medium, the proposed approach offers a promising pathway towards decarbonised heating systems, especially in regions with favourable solar availability during non-heating seasons.

Author agreement statement

We the undersigned declare that this manuscript is original, has not been published before and is not currently being considered for publication elsewhere.

We confirm that the manuscript has been read and approved by all named authors and that there are no other persons who satisfied the criteria for authorship but are not listed. We further confirm that the order of authors listed in the manuscript has been approved by all of us.

We understand that the Corresponding Author is the sole contact for the Editorial process. He/she is responsible for communicating with the other authors about progress, submissions of revisions and final approval of proofs

CRediT authorship contribution statement

Sandeep Bandarwadkar: Writing – review & editing, Writing – original draft, Visualization, Validation, Supervision, Resources, Methodology, Investigation, Formal analysis, Data curation, Conceptualization. **Tadas Zdankus:** Writing – review & editing, Writing – original draft, Validation, Supervision, Resources, Methodology, Investigation, Formal analysis, Data curation, Conceptualization. **Rokas Valancius:** Methodology, Investigation, Formal analysis. **Paul Christodoulides:** Writing – review & editing, Funding acquisition. **Lazaros Aresti:** Writing – review & editing, Investigation, Formal analysis.

Funding

The work presented in this paper has been undertaken in the framework of the research project SMALL SCALE INFRASTRUCTURES/ 1222/0234, which is implemented under the programme of social cohesion “THALIA 2021–2027” co-funded by the European Union, through Research and Innovation Foundation.

Declaration of Competing Interest

The authors declare that they have no known competing financial interests or personal relationships that could have appeared to influence the work reported in this paper.

Data Availability

Data will be made available on request.

References

“Applications: Tube, Pipe & Fittings: Copper Tube Handbook: III. Solar Energy Systems.” Accessed: Jul. 19, 2025. [Online]. Available: ⟨https://copper.org/applications/plumbing/cth/design-installation/cth_3design_solar.php⟩.

“Computational modelling of a ground heat exchanger with groundwater flow.” Accessed: Mar. 31, 2025. [Online]. Available: ⟨https://www.researchgate.net/publication/315794624_Computational_modelling_of_a_ground_heat_exchanger_with_groundwater_flow⟩.

“EN 12975-1:2006 - Thermal solar systems and components - Solar collectors - Part 1: General.” Accessed: Aug. 20, 2025. [Online]. Available: ⟨https://standards.iteh.ai/catalog/standards/cen/56f8d8b4-543c-45ee-aefc-2dc4b3acd92a/en-12975-1-2006⟩.

“Executive summary – Electricity Market Report 2023 – Analysis - IEA.” Accessed: Mar. 31, 2025. [Online]. Available: ⟨https://www.iea.org/reports/electricity-market-report-2023/executive-summary⟩.

“Global electricity demand growth is slowing, weighed down by economic weakness and high prices - News - IEA.” Accessed: Mar. 31, 2025. [Online]. Available: ⟨https://www.iea.org/news/global-electricity-demand-growth-is-slowing-weighed-down-by-economic-weakness-and-high-prices⟩.

“GUIDE TO STANDARD ISO 9806:2017 A Resource for Manufacturers, Testing Laboratories, Certification Bodies and Regulatory Agencies,”, 2018. https://doi.org/10.13140/RG.2.2.27725.08168.

“Heat Transfer Fluids for Solar Water Heating Systems | Department of Energy.” Accessed: Mar. 31, 2025. [Online]. Available: ⟨https://www.energy.gov/energysaver/heat-transfer-fluids-solar-water-heating-systems⟩.

“Home - Lithuanian Geological Survey under the Ministry of Environment.” Accessed: Jun. 18, 2025. [Online]. Available: ⟨https://lgt.lrv.lt/en/⟩.

“Housing - Oficialiosios statistikos portalas.” Accessed: Mar. 31, 2025. [Online]. Available: ⟨https://osp.stat.gov.lt/en/lietuvos-statistikos-metrastis/lsm-2019/gyventojai-ir-socialine-statistika/bustas⟩.

“IEA SHC || Task 26 || IEA SHC || Task 26.” Accessed: Aug. 20, 2025. [Online]. Available: ⟨https://task26.iea-shc.org/⟩.

“JRC Photovoltaic Geographical Information System (PVGIS) - European Commission.” Accessed: Jul. 25, 2025. [Online]. Available: ⟨https://re.jrc.ec.europa.eu/pvg_tools/en/⟩.

“Kaunas June Weather, Average Temperature (Lithuania) - Weather Spark.” Accessed: Mar. 31, 2025. [Online]. Available: ⟨https://weatherspark.com/m/90350/6/Average-Weather-in-June-in-Kaunas-Lithuania⟩.

“Large Scale solar heating in Marstal.” Accessed: Mar. 31, 2025. [Online]. Available: ⟨https://stateofgreen.com/en/solutions/large-scale-solar-heating-in-marstal⟩.

“Large-scale thermal storage pit.” Accessed: Mar. 31, 2025. [Online]. Available: ⟨https://stateofgreen.com/en/solutions/large-scale-thermal-pit-storage⟩.

“Net Zero by 2050: A Roadmap for the Global Energy Sector”, Accessed: Sep. 06, 2025. [Online]. Available: ⟨www.iea.org/t&c/⟩.

“PVGIS data sources & calculation methods - European Commission.” Accessed: Jul. 27, 2025. [Online]. Available: ⟨https://joint-research-centre.ec.europa.eu/photovoltaic-geographical-information-system-pvgis/getting-started-pvgis/pvgis-data-sources-calculation-methods⟩.

“Solar Tilt Angle: How To Find The Best Panel Position.” Accessed: Aug. 20, 2025. [Online]. Available: ⟨https://www.sunhub.com/blog/solar-tilt-angle-guide/⟩.

“Technical Regulations for Construction, STR 2.01.02:2016, Energy Performance Design and Certification of Buildings”. Accessed: April 25, 2025. [Online]. Available: ⟨https://e-seimas.lrs.lt/portal/legalAct/lt/TAD/15767120a80711e68987e8320e9a5185/asr⟩.

“Technical Regulations for Construction, STR 2.01.12:2024, Construction Climatology". Accessed: April 25, 2025. [Online]. Available: ⟨https://e-seimas.lrs.lt/portal/legalAct/lt/TAD/60c1acd17f6311ef84ff9693ecd03ff5?jfwid=e5xndzg76⟩.

“Technology Position Paper Compact Thermal Energy Storage,” 2023, doi: 10.18777/ieashc-task67-2023-0001.

“TOUGH: Suite of Simulators for Nonisothermal Multiphase Flow and Transport in Fractured Porous Media - TOUGH.” Accessed: Mar. 31, 2025. [Online]. Available: ⟨https://tough.lbl.gov⟩.

“Tripling renewable power and doubling energy efficiency by 2030: Crucial steps towards 1.5°C.” Accessed: Mar. 31, 2025. [Online]. Available: ⟨https://www.irena.org/Digital-Report/Tripling-renewable-power-and-doubling-energy-efficiency-by-2030⟩.

“User Manual for GeoSIAM Software Version 2.0 - RSE.” Accessed: Mar. 31, 2025. [Online]. Available: ⟨https://www.rse-web.it/rapporti/18002366/⟩.

"Yonos PICO 15/1-4 | Wilo." Accessed: Feb. 05, 2026. [Online]. Available: ⟨https://wilo.com/gb/en/Products/en/products-expertise/wilo-yonos-pico/yonos-pico-15-1-4⟩.

2016 *7th India International Conference on Power Electronics (IICPE)*. IEEE, 2016.

Abu-Hamdeh, N.H., Reeder, R.C., 2000a. Soil thermal conductivity effects of density, moisture, salt concentration, and organic matter. Soil Sci. Soc. Am. J. 64 (4), 1285–1290. https://doi.org/10.2136/SSSAJ2000.6441285X.

Abu-Hamdeh, N.H., Reeder, R.C., 2000b. Soil thermal conductivity effects of density, moisture, salt concentration, and organic matter. Soil Sci. Soc. Am. J. 64 (4), 1285–1290. https://doi.org/10.2136/sssaj2000.6441285x (subpage:string: full).

Ahmadfard, M., Baniasadi, E., 2025. Borehole thermal energy storage systems: a comprehensive review using bibliometric and qualitative tools. Appl. Energy 387. https://doi.org/10.1016/J.APENERGY.2025.125638.

Allen, R., Pereira, L., Raes, D., Smith, M., "Parte, C., 2006. Evapotranspiración del cultivo en condiciones no estándar ET c bajo condiciones de estrés hídrico," *Evapotranspiración del cultivo: Guías para la determinación de los requerimientos de agua de los cultivos*. ESTUDIO FAO RIEGO Y Dren. 56, 48.

Arabkoohsar, A., 2023. Classification of energy storage systems (Jan). Future GridScale Energy Storage Solut. Mech. Chem. Technol. Princ. 1–30. https://doi.org/10.1016/B978-0-323-90786-6.00011-X.

Aresti, L., et al., 2024. Energy geo-structures: A review of their integration with other sources and its limitations (Sep). Renew. Energy 230, 120835. https://doi.org/10.1016/J.RENENE.2024.120835.

Aresti, L., Christodoulides, P., Panayiotou, G.P., Florides, G., 2020. The potential of utilizing buildings' foundations as thermal energy storage (TES) units from solar plate collectors (Jun). Energ. (Basel) 13 (11). https://doi.org/10.3390/EN13112695.

Bao, H., Ma, Z., 2022. Thermochemical energy storage. Storing Energy 651–683. https://doi.org/10.1016/B978-0-12-824510-1.00028-3.

T.L. Bergman, A.S. Lavine, and F.P. Incropera, "Fundamentals of Heat and Mass Transfer," p. 1076, 2011, Accessed: Nov. 13, 2025. [Online]. Available: ⟨https://books.google.com/books/about/Fundamentals_of_Heat_and_Mass_Transfer_7.html?hl=lt&id=5cgbAAAAQBAJ⟩.

Bogdanov, D., et al., 2021. Low-cost renewable electricity as the key driver of the global energy transition towards sustainability (Jul). Energy 227, 120467. https://doi.org/10.1016/J.ENERGY.2021.120467.

Bolton, R., Cameron, L., Kerr, N., Winskel, M., Desguers, T., 2023. Seasonal thermal energy storage as a complementary technology: case study insights from Denmark and The Netherlands (Dec). J. Energy Storage 73, 109249. https://doi.org/10.1016/J.EST.2023.109249.

Brown, C.S., et al., 2024. Assessing the technical potential for underground thermal energy storage in the UK (Jul). Renew. Sustain. Energy Rev. 199, 114545. https://doi.org/10.1016/J.RSER.2024.114545.

S. Chapuis and M. Bernier, "Seasonal storage of solar energy in borehole heat exchangers," in Proceedings of the 11th International IBPSA Conference – Building Simulation 2009, Glasgow, U.K., Jul. 2009, pp. 599–606.

Duuzaamloket," Solar collector energy label values," Technical Datasheet DS_3645.2017. [online]. Available: ⟨https://www.duurzaamloket.nl/DBF/PDF_Downloads/DS_3645⟩.

Dundulis, K., Gadeikis, S., Gadeikytė, S., Račkauskas, V., 2006. In: Dundulis, K., Gadeikis, S., Gadeikytė, S., Račkauskas, V. (Eds.), Geologija, no 53, 47–51.

Fan, J., Shah, L.J., Furbo, S., 2007. Flow distribution in a solar collector panel with horizontally inclined absorber strips. Sol. Energy 81 (12), 1501–1511. https://doi.org/10.1016/J.SOLENER.2007.02.001.

Fleuchaus, P., Godschalk, B., Stober, I., Blum, P., 2018. Worldwide application of aquifer thermal energy storage – A review. Renew. Sustain. Energy Rev. 94, 861–876. https://doi.org/10.1016/J.RSER.2018.06.057.

Gabrielsson, A., Bergdahl, U., Moritz, L., 2000. Thermal energy storage in soils at temperatures reaching 90°C (Feb). J. Sol. Energy Eng. 122 (1), 3–8. https://doi.org/10.1115/1.556272.

W. Gao, M. Qadrdan, M. Chaudry, and J. Wu, "Seasonal Storage of Heat in Boreholes: Technical Note," 2023.

Hua, W., Lv, X., Zhang, X., Ji, Z., Zhu, J., 2023. Research progress of seasonal thermal energy storage technology based on supercooled phase change materials. J. Energy Storage 67, 107378. https://doi.org/10.1016/J.EST.2023.107378.

I. Renewable Energy Agency, "Innovation Outlook Thermal Energy Storage About IRENA," 2020, Accessed: Nov. 12, 2025. [Online]. Available: ⟨www.irena.org⟩.

Ji, H.Y., Kang, C., Park, D., 2024. Experiment and prediction analysis of thermal energy storage for heat load balancing in domestic hot water system. Energy 313, 134040. https://doi.org/10.1016/J.ENERGY.2024.134040.

Jouhara, H., Żabnieńska-Góra, A., Khordehgah, N., Ahmad, D., Lipinski, T., 2020. Latent thermal energy storage technologies and applications: A review. Int. J. Thermofluids 5–6, 100039. https://doi.org/10.1016/J.IJFT.2020.100039.

Jradi, M., Veje, C., Jørgensen, B.N., 2017. Performance analysis of a soil-based thermal energy storage system using solar-driven air-source heat pump for Danish buildings sector. Appl. Therm. Eng. 114, 360–373. https://doi.org/10.1016/J.APPLTHERMALENG.2016.12.005.

Kalogirou, S.A., 2004. Solar thermal collectors and applications. Prog. Energy Combust. Sci. 30 (3), 231–295. https://doi.org/10.1016/J.PECS.2004.02.001.

Koçak, B., Fernandez, A.I., Paksoy, H., 2020. Review on sensible thermal energy storage for industrial solar applications and sustainability aspects. Sol. Energy 209, 135–169. https://doi.org/10.1016/J.SOLENER.2020.08.081.

Kveselis, V., Lisauskas, A., Farida Dzenajavičienė, E., 2014. Investigating possibilities to integrate solar heat into district heating systems of Lithuanian towns. 9th Int. Conf. Environ. Eng. ICEE 2014 Dept. Math. Model. https://doi.org/10.3846/enviro.2014.268.

Lanahan, M., Tabares-Velasco, P.C., 2017. Seasonal Thermal-Energy Storage: A Critical Review on BTES Systems, Modeling, and System Design for Higher System Efficiency. *2017, Vol. 10, Page 743* Energies 10 (6), 743. https://doi.org/10.3390/EN10060743.

D. Mangold and L. Deschaintre, "Task 45 Large Systems Seasonal thermal energy storage Report on state of the art and necessary further R+D page 1 / 48 Subject: Seasonal thermal energy storage," 2015, Accessed: Nov. 12, 2025. [Online]. Available: ⟨www.solites.de⟩.

Pourahmadiyan, A., Sadi, M., Arabkoohsar, A., 2023. Seasonal thermal energy storage. Future GridScale Energy Storage Solut. Mech. Chem. Technol. Princ. 215–267. https://doi.org/10.1016/B978-0-323-90786-6.00013-3.

Pruess, K., 2004. The TOUGH Codes—a family of simulation tools for multiphase flow and transport processes in permeable media. Vadose Zone J. 3 (3), 738–746. https://doi.org/10.2136/VZJ2004.0738.

Sadeghi, H., Jalali, R., Singh, R.M., 2024. A review of borehole thermal energy storage and its integration into district heating systems. Renew. Sustain. Energy Rev. 192. https://doi.org/10.1016/J.RSER.2023.114236.

Saleem, Y., Sajid, J., Ahmed, N., 2022. The Thermal Analysis of a Sensible Heat Thermal Energy Storage System Using Circular-Shaped Slag and Concrete for Medium- to High-Temperature Applications. *Vol. 12, Page 99* Eng. Proc. 2021 12 (1), 99. https://doi.org/10.3390/ENGPROC2021012099.

Salunkhe, P.B., Jaya Krishna, D., 2017. Investigations on latent heat storage materials for solar water and space heating applications. J. Energy Storage 12, 243–260. https://doi.org/10.1016/J.EST.2017.05.008.

Sarbu, I., Sebarchievici, C., 2018. A comprehensive review of thermal energy storage. *2018, Vol. 10, Page 191* Sustainability 10 (1), 191. https://doi.org/10.3390/SU10010191.

Sass, I., Krusemark, M., Seib, L., Bossennec, C., Pham, T.H., Schedel, M., Weydt, L., Buness, H., Homuth, B., Feb. 2024. Medium-Deep Borehole Thermal Energy Storage (MD-BTES): From exploration to district-heating grid connection – Insights from SKEWS and PUSH-IT projects. Stanford Univ, Stanford, CA, USA.

Seyitini, L., Belgasim, B., Enweremadu, C.C., 2023. Solid state sensible heat storage technology for industrial applications – A review (Jun). J. Energy Storage 62, 106919. https://doi.org/10.1016/J.EST.2023.106919.

Sibbitt, B., et al., 2012. The performance of a high solar fraction seasonal storage district heating system – five years of operation. Energy Procedia 30, 856–865. https://doi.org/10.1016/J.EGYPRO.2012.11.097.

SP Technical Research Institute of Sweden, 2010. Description of ScenoCalc (Solar Collector Energy Output Calculator): A Program for Calculation of Annual Solar Collector Energy Output. Borås, Sweden.

Steinmann, W.D., 2021. Thermal energy storage for medium and high temperatures: concepts and applications. Therm. Energy Storage Medium High. Temp. Concepts Appl. 1–395. https://doi.org/10.1007/978-3-658-02004-0.

Stemmle, R., et al., 2024. Policies for aquifer thermal energy storage: international comparison, barriers and recommendations. Clean. Technol. Environ. Policy. https://doi.org/10.1007/S10098-024-02892-1.

Tawalbeh, M., Khan, H.A., Al-Othman, A., Almomani, F., Ajith, S., 2023. A comprehensive review on the recent advances in materials for thermal energy storage applications. Int. J. Thermofluids 18, 100326. https://doi.org/10.1016/J.IJFT.2023.100326.

Vahidhosseini, S.M., Rashidi, S., Hsu, S.H., Yan, W.M., Rashidi, A., 2024. Integration of solar thermal collectors and heat pumps with thermal energy storage systems for building energy demand reduction: A comprehensive review. J. Energy Storage 95, 112568. https://doi.org/10.1016/J.EST.2024.112568.

G. Sarlos *et al.*, (n.d) "Laboratoire de systèmes énergétiques (lasen) heat storage in the ground duct ground heat storage model for trnsys (trnvdst) User manual for the October 1996 version".

A. María and T. Huld, "Performance comparison of different models for the estimation of global irradiance on inclined surfaces," European Commission, Joint Research Centre (JRC), Luxembourg, 2013. doi: 10.2790/91554.

W.R. Walker, J.D. Sabey, and D.R. Hampton, "Studies of heat transfer and water migration in soils: Final Report," 1979.

Xiang, Y., Xie, Z., Furbo, S., Wang, D., Gao, M., Fan, J., 2022. A comprehensive review on pit thermal energy storage: technical elements, numerical approaches and recent applications. J. Energy Storage 55. https://doi.org/10.1016/J.EST.2022.105716.

Xiong, K., et al., 2023. A new model to predict soil thermal conductivity. *2023 13:1* Sci. Rep. 13 (1), 1–14. https://doi.org/10.1038/s41598-023-37413-5.

Xu, K., Du, M., Hao, L., Mi, J., Yu, Q., Li, S., 2020. A review of high-temperature selective absorbing coatings for solar thermal applications. J. Mater. 6 (1), 167–182. https://doi.org/10.1016/J.JMAT.2019.12.012.

Yang, T., Liu, W., Kramer, G.J., Sun, Q., 2021. Seasonal thermal energy storage: A techno-economic literature review (Apr). Renew. Sustain. Energy Rev. 139, 110732. https://doi.org/10.1016/J.RSER.2021.110732.

Zhang, L., Xu, P., Mao, J., Tang, X., Li, Z., Shi, J., 2015b. A low cost seasonal solar soil heat storage system for greenhouse heating: Design and pilot study. Appl. Energy 156, 213–222. https://doi.org/10.1016/J.APENERGY.2015.07.036.

Zhang, L., Xu, P., Mao, J., Tang, X., Li, Z., Shi, J., 2015a. A low cost seasonal solar soil heat storage system for greenhouse heating: design and pilot study (Oct). Appl. Energy 156, 213–222. https://doi.org/10.1016/J.APENERGY.2015.07.036.

Zhou, J., Cui, Z., Xu, F., Zhang, G., 2021. Performance analysis of solar-assisted ground-coupled heat pump systems with seasonal thermal energy storage to supply domestic hot water for campus buildings in Southern China. *2021, Vol. 13, Page 8344* Sustainability 13 (15), 8344. https://doi.org/10.3390/SU13158344.